ARTICLES
https://doi.org/10.1038/s41590-021-00895-4

nature immunology

Blockade of IL-22 signaling reverses erythroid dysfunction in stress-induced anemias

Mahesh Raundhal[1,2,3]✉, Shrestha Ghosh[1,2,3], Samuel A. Myers[4], Michael S. Cuoco[5], Meromit Singer[2,4,6], Steven A. Carr[4], Sushrut S. Waikar[7,8], Joseph V. Bonventre[7], Jerome Ritz[9], Richard M. Stone[9], David P. Steensma[9], Aviv Regev[5,10,11] and Laurie H. Glimcher[1,2,3]✉

Patients with myelodysplastic syndromes (MDSs) display severe anemia but the mechanisms underlying this phenotype are incompletely understood. Right open-reading-frame kinase 2 (*RIOK2*) encodes a protein kinase located at 5q15, a region frequently lost in patients with MDS del(5q). Here we show that hematopoietic cell-specific haploinsufficient deletion of *Riok2* (*Riok2*$^{f/+}$*Vav1*^{cre}) led to reduced erythroid precursor frequency leading to anemia. Proteomic analysis of *Riok2*$^{f/+}$*Vav1*^{cre} erythroid precursors suggested immune system activation, and transcriptomic analysis revealed an increase in p53-dependent interleukin (IL)-22 in *Riok2*$^{f/+}$*Vav1*^{cre} CD4$^+$ T cells (T_H22). Further, we discovered that the IL-22 receptor, IL-22RA1, was unexpectedly present on erythroid precursors. Blockade of IL-22 signaling alleviated anemia not only in *Riok2*$^{f/+}$*Vav1*^{cre} mice but also in wild-type mice. Serum concentrations of IL-22 were increased in the subset of patients with del(5q) MDS as well as patients with anemia secondary to chronic kidney disease. This work reveals a possible therapeutic opportunity for reversing many stress-induced anemias by targeting IL-22 signaling.

MDSs are a group of cancers characterized by failure of blood cells in the bone marrow to mature. About 7 out of 100,000 people are affected and the typical survival time following diagnosis is less than 3 years. While a sizable percentage of MDS cases progress to acute myelogenous leukemia (AML), most of the morbidity and mortality associated with MDSs results not from transformation to AML but rather from hematological cytopenias.

Anemia is the most common hematologic manifestation of MDSs, particularly in the subset of patients with del(5q) MDS. Del(5q), either isolated or accompanied by additional cytogenetic abnormalities, is the most commonly detected chromosomal abnormality in MDSs, reported in 10–15% of patients[1–4]. The severe anemia in patients with del(5q) MDSs has been linked to haploinsufficiency of ribosomal proteins such as RPS14 and RPS19 (refs. [5,6]). Previous studies using mice with haploinsufficient 5q gene deletions revealed diminished erythroid progenitor frequency[7–10] but the mechanisms underlying this phenotype are incompletely understood. *RIOK2* encodes an atypical serine–threonine protein kinase with an indispensable function as a component of the pre-40S ribosome subunit[11].

There is growing evidence for the role of activated innate immunity and inflammation as well as immune dysregulation in the pathogenesis of MDSs[12–15]. Abnormal expression of numerous cytokines has been reported in MDSs[16–19]. Chronic immune stimulation in both hematopoietic stem and progenitor cells and the bone marrow (BM) microenvironment[20] was suggested to be central to the pathogenesis of MDSs. In patients with chronic inflammation, cytokines in the BM have been associated with inhibition of erythropoiesis[21]. Despite growing evidence for a link between the immune system and MDS pathogenesis, no study has identified the mechanism by which the immune microenvironment may initiate or contribute to the MDS phenotype. Further it remains unclear how ribosomal protein haploinsufficiency is connected with the immune system in MDSs.

Results

***Riok2* haploinsufficiency leads to anemia.** We previously noted that *Riok2* expression was reduced in T cells lacking the endoplasmic reticulum stress transcription factor Xbp1 (ref. [22]). RIOK2 is a little-studied atypical serine–threonine protein kinase[23] encoded by *RIOK2* at 5q15 in the human genome (Extended Data Fig. 1a), adjacent to the 5q commonly deleted regions in MDSs and frequently lost in MDSs and acute myeloid leukemia[24–27].Gene expression commons (GEXC)[28] analysis revealed that in mouse BM, *Riok2* expression is highest in primitive colony-forming-unit erythroid (CFU-e) cells, suggesting that RIOK2 may be involved in maintaining red blood cell (RBC) output (Extended Data Fig. 1d). To further study the role of RIOK2 in hematopoiesis, we generated *Vav1-Cre* transgenic floxed *Riok2* (*Riok2*$^{f/+}$*Vav1*^{cre}) mice in which cre recombinase is under the control of the hematopoietic cell-specific *Vav1* promoter. *Riok2* floxed mice were generated with exons 5 and 6 flanked by *loxP* sites (Extended Data Fig. 1b,c). Notably, no Vav1-Cre floxed *Riok2* homozygous-deficient mice (*Riok2*$^{f/f}$*Vav1*^{cre}) were recovered (Extended Data Fig. 1f), indicating embryonic lethality from complete hematopoietic deletion of *Riok2*. However, heterozygous *Riok2*$^{f/+}$*Vav1*^{cre} mice were viable with approximately

[1]Department of Cancer Immunology and Virology, Dana-Farber Cancer Institute, Boston, MA, USA. [2]Department of Immunology, Harvard Medical School, Boston, MA, USA. [3]Department of Medicine, Brigham and Women's Hospital, Boston, MA, USA. [4]Broad Institute of MIT and Harvard, Cambridge, MA, USA. [5]Klarman Cell Observatory, Broad Institute of Harvard and MIT, Cambridge, MA, USA. [6]Department of Data Sciences, Dana-Farber Cancer Institute, Boston, MA, USA. [7]Renal Division, Department of Medicine, Brigham and Women's Hospital, Harvard Medical School, Boston, MA, USA. [8]Renal Section, Boston University Medical Center, Boston, MA, USA. [9]Department of Medical Oncology, Dana-Farber Cancer Institute, Harvard Medical School, Boston, MA, USA. [10]Howard Hughes Medical Institute, Chevy Chase, MD, USA. [11]Koch Institute for Integrative Cancer Research, Department of Biology, Massachusetts Institute of Technology, Cambridge, MA, USA. ✉e-mail: Mahesh_Raundhal@dfci.harvard.edu; Laurie_Glimcher@dfci.harvard.edu

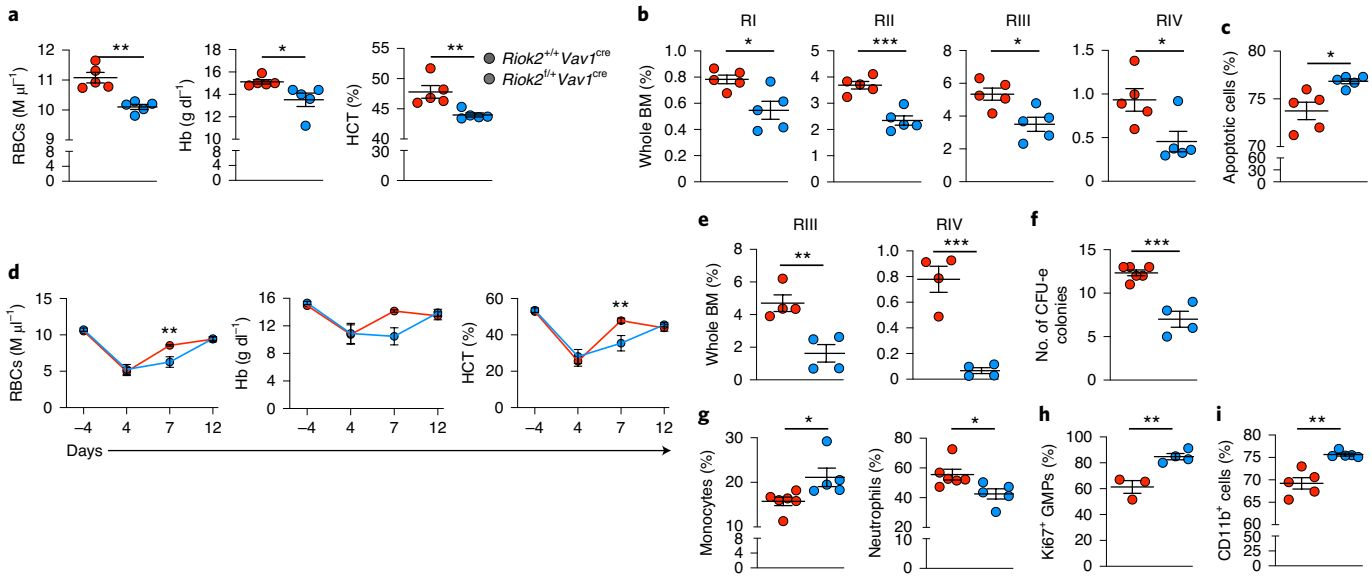

Fig. 1 | *Riok2*-haploinsufficient (*Riok2*$^{f/+}$*Vav1*^{cre}) mice display anemia and myeloproliferation. a, PB RBC numbers, Hb and HCT in *Riok2*$^{f/+}$*Vav1*^{cre} mice in comparison to *Riok2*$^{+/+}$*Vav1*^{cre} controls ($n=5$ per group). **b**, Frequency of erythroid progenitor/precursor populations among viable BM cells in *Riok2*$^{f/+}$*Vav1*^{cre} mice and *Riok2*$^{+/+}$*Vav1*^{cre} controls ($n=5$ per group). **c**, Frequency of apoptotic erythroid precursors among viable BM cells in *Riok2*$^{f/+}$*Vav1*^{cre} mice and *Riok2*$^{+/+}$*Vav1*^{cre} controls ($n=5$ per group). **d**, PB RBC numbers, Hb and HCT in *Riok2*$^{f/+}$*Vav1*^{cre} mice and *Riok2*$^{+/+}$*Vav1*^{cre} controls undergoing phenylhydrazine (PhZ)-induced stress erythropoiesis ($n=7$ per group). **e**, Frequency of RIII and RIV erythroid precursor populations among viable BM cells in *Riok2*$^{f/+}$*Vav1*^{cre} mice and *Riok2*$^{+/+}$*Vav1*^{cre} controls 6 d after PhZ treatment ($n=4$ per group). **f**, Number of CFU-e colonies in Epo-containing MethoCult assay using Lin$^-$c-kit$^+$CD71$^+$ cells from *Riok2*$^{f/+}$*Vav1*^{cre} mice ($n=4$) in comparison to *Riok2*$^{+/+}$*Vav1*^{cre} controls ($n=6$). **g**, Percentage of monocytes (CD11b$^+$Ly6G$^-$Ly6C^{hi}) and neutrophils (CD11b$^+$Ly6G$^+$) in the PB of *Riok2*$^{f/+}$*Vav1*^{cre} mice ($n=6$) in comparison to *Riok2*$^{+/+}$*Vav1*^{cre} controls ($n=5$). **h**, Percentage of Ki67$^+$ GMPs in the BM of *Riok2*$^{f/+}$*Vav1*^{cre} mice ($n=3$) and *Riok2*$^{+/+}$*Vav1*^{cre} controls ($n=4$). **i**, Percentage of CD11b$^+$ cells obtained from Lin$^-$Sca-1$^+$c-kit$^+$ BM cells from *Riok2*$^{f/+}$*Vav1*^{cre} mice and *Riok2*$^{+/+}$*Vav1*^{cre} controls cultured in MethoCult for 7 d ($n=5$ per group). Unpaired two-tailed Student's *t*-test (**a**–**c**,**e**–**i**) and one-way analysis of variance (ANOVA) with Tukey's correction for multiple comparisons (**d**) was used to calculate statistical significance. $^*P<0.05$, $^{**}P<0.01$, $^{***}P<0.001$. Data are shown as mean ± s.e.m and are representative of two (**c**,**d**,**f**–**h**) or three (**a**,**b**,**e**,**i**) independent experiments.

50% *Riok2* mRNA expression in hematopoietic cells compared to that of *Vav1*^{cre} controls (Extended Data Fig. 1e). As seen with other ribosomal protein haploinsufficiency mouse models[10], BM cells from *Riok2*$^{f/+}$*Vav1*^{cre} mice showed reduced nascent protein synthesis in vivo compared to *Vav1*^{cre} controls (Extended Data Fig. 1g), consistent with a RIOK2 role in maturation of the pre-40S ribosome. A recent study[29] showed that ribosomal protein deficiency-mediated reduced protein synthesis predominantly affects erythropoiesis over myelopoiesis.

Consistent with the high expression of *Riok2* in primitive CFU-e cells in the BM, aged (>60 weeks) mice with heterozygous deletion of *Riok2* in hematopoietic cells (*Riok2*$^{f/+}$*Vav1*^{cre}) displayed anemia with reduced peripheral blood (PB) RBC numbers, hemoglobin (Hb) and hematocrit (HCT) (Fig. 1a). We next determined whether *Riok2* haploinsufficiency-mediated anemia was secondary to a defect in erythroid development in the BM, the major site of erythropoiesis. We characterized the stages (referred to here as RI, RII, RIII and RIV) of erythropoiesis by flow cytometry using the expression of Ter119 and CD71 (Extended Data Fig. 2a). *Riok2*$^{f/+}$*Vav1*^{cre} mice had impaired erythropoiesis in the BM (Fig. 1b and Extended Data Fig. 2b). Moreover, *Riok2* haploinsufficiency led to increased apoptosis in erythroid precursors compared to controls (Fig. 1c). Additionally, *Riok2*$^{f/+}$*Vav1*^{cre} erythroid precursors showed a decrease in cell quiescence with cell cycle block at the G1 phase (Extended Data Fig. 2c). A block in cell cycle is driven by a group of proteins known as cyclin-dependent kinase inhibitors (CKIs). The expression of p21 (a CKI encoded by *Cdkn1a*) was increased in erythroid precursors from *Riok2*$^{f/+}$*Vav1*^{cre} mice compared to *Riok2*$^{+/+}$*Vav1*^{cre} controls (Extended Data Fig. 2d).

We next examined the effect of *Riok2* haploinsufficiency on stress-induced erythropoiesis using 8–12-week-old mice in which hemolysis was induced by nonlethal phenylhydrazine treatment (25 mg per kg (body weight) on days 0 and 1). After acute hemolytic stress, *Riok2*$^{f/+}$*Vav1*^{cre} mice developed more severe anemia and had a delayed RBC recovery response compared to *Riok2*$^{+/+}$*Vav1*^{cre} control mice (Fig. 1d) and succumbed faster to a lethal dose of phenylhydrazine (35 mg per kg on days 0 and 1) compared to *Vav1*^{cre} controls (Extended Data Fig. 2e). The anemia in young phenylhydrazine-administered *Riok2*$^{f/+}$*Vav1*^{cre} mice seen on day 7 was preceded by a reduction in BM RIII and RIV erythroid precursor frequency on day 6, highlighting an erythroid differentiation defect in Riok2-haploinsufficient mice (Fig. 1e and Extended Data Fig. 2f). In line with a role for RIOK2 in driving erythroid differentiation, fewer CFU-e colonies were observed in erythropoietin-containing MethoCult cultures from *Riok2*-haploinsufficient Lin$^-$c-kit$^+$CD71$^+$ cells compared to *Riok2*-sufficient cells (Fig. 1f). To determine whether *Riok2* haploinsufficiency in BM cells drives anemia, we generated BM chimeras. Wild-type (WT) mice transplanted with *Riok2*$^{f/+}$*Vav1*^{cre} whole BM developed anemia compared to *Riok2*$^{+/+}$*Vav1*^{cre} BM transplanted WT mice (Extended Data Fig. 2g). In addition, tamoxifen-inducible deletion of *Riok2* in *Riok2*$^{f/+}$*Ert2*^{cre} mice led to reduction in PB RBCs, Hb and HCT compared to *Riok2*$^{+/+}$*Ert2*^{cre} controls (Extended Data Fig. 2h). Taken together, these data show that *Riok2* haploinsufficiency leads to anemia owing to defective BM erythroid differentiation.

***Riok2* haploinsufficiency increases myelopoiesis.** In addition to the reduction in RBC numbers in PB from aged *Riok2*$^{f/+}$*Vav1*^{cre} mice, we also observed an increased percentage of monocytes

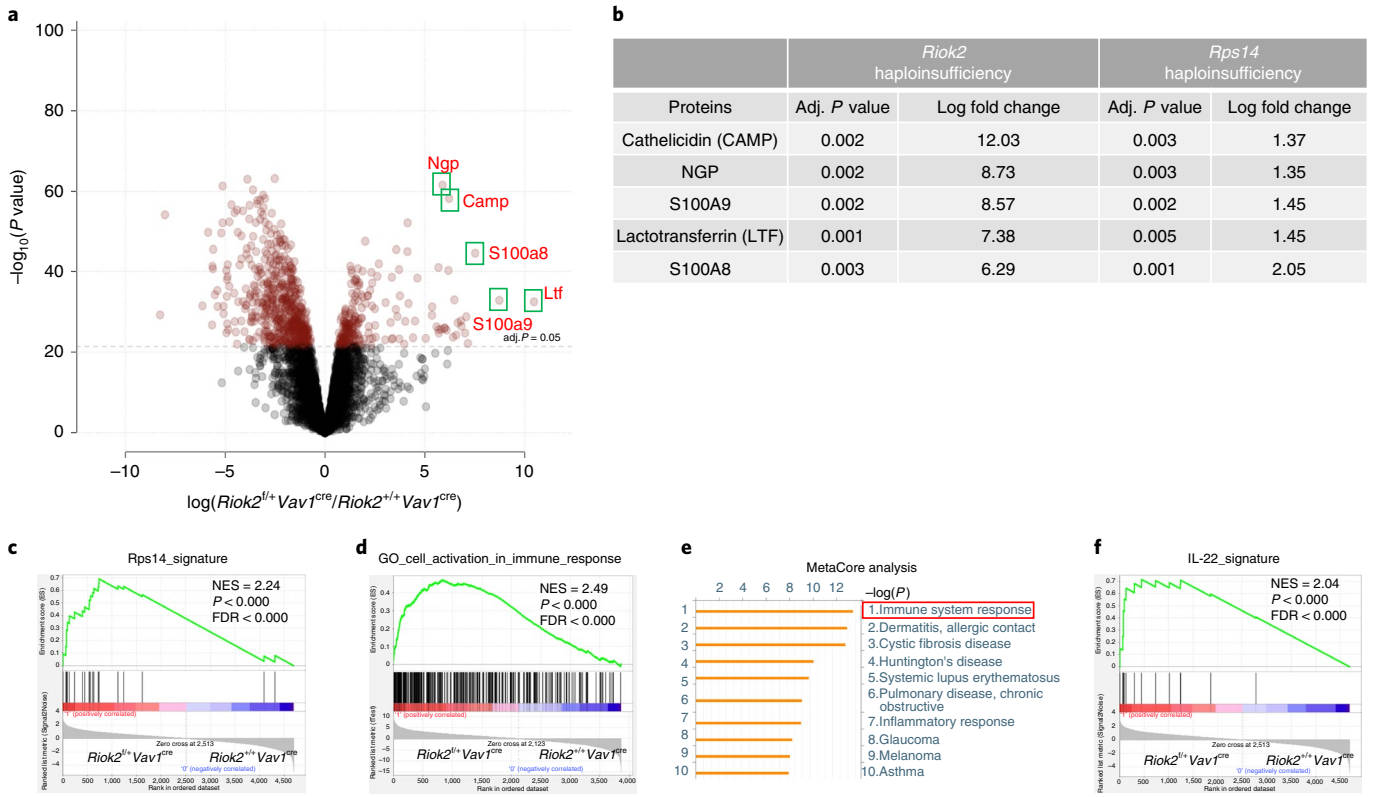

	Riok2 haploinsufficiency		*Rps14* haploinsufficiency	
Proteins	Adj. *P* value	Log fold change	Adj. *P* value	Log fold change
Cathelicidin (CAMP)	0.002	12.03	0.003	1.37
NGP	0.002	8.73	0.003	1.35
S100A9	0.002	8.57	0.002	1.45
Lactotransferrin (LTF)	0.001	7.38	0.005	1.45
S100A8	0.003	6.29	0.001	2.05

Fig. 2 | Quantitative proteomics of *Riok2*-haploinsufficient erythroid precursors reveals immune activation signatures. a, Proteomic analysis of changes in protein expression in erythroid progenitors from *Riok2*-haploinsufficient mice and *Vav1*^{cre} controls ($n = 4$–5 mice per group). **b**, Comparison of upregulated proteins with their respective *P* values and log fold-change values in erythroid precursors from *Riok2*-haploinsufficient mice and *Rps14* haploinsufficient mice with their respective controls. **c**,**d**,**f**, GSEA performed on proteomics data shown in **a** to reveal similarity with *Rps14* haploinsufficient data (**c**), activation of immune response (**d**) and enrichment of IL-22 signature genes (**f**). NES, normalized enrichment score; FDR, false discovery rate. **e**, MetaCore analysis of the Riok2 proteomics dataset shown in **a**. A two-sample moderated Student's *t*-test with multiple hypothesis corrections was used to calculate statistical significance in **b**.

(monocytosis) and decreased percentage of neutrophils (neutropenia) compared to controls (Fig. 1g and Extended Data Fig. 2i). Granulocyte–macrophage progenitors (GMPs) in the BM give rise to PB myeloid cells. The percentage of proliferating (Ki67$^+$) GMPs in the BM was increased in *Riok2*$^{f/+}$*Vav1*^{cre} mice compared to *Riok2*$^{+/+}$*Vav1*^{cre} controls (Fig. 1h and Extended Data Fig. 2j). To analyze the effect of *Riok2* haploinsufficiency on myelopoiesis in the absence of in vivo compensatory mechanisms, we cultured LSK (lineage$^-$Sca-1$^+$Kit$^+$) cells from the BM of *Riok2*$^{f/+}$*Vav1*^{cre} and *Riok2*$^{+/+}$*Vav1*^{cre} controls in a MethoCult assay supplemented with growth factors (IL-6, IL-3, stem cell factor but devoid of erythropoietin). LSKs from *Riok2*$^{f/+}$*Vav1*^{cre} mice gave rise to an increased percentage of CD11b$^+$ myeloid cells (Fig. 1i and Extended Data Fig. 2k), suggesting a cell-intrinsic myeloproliferative effect due to *Riok2* haploinsufficiency consistent with a myelodysplasia phenotype.

We also evaluated whether *Riok2* haploinsufficiency affects early hematopoietic progenitors. Frequency and numbers of early hematopoietic progenitors were comparable between young *Riok2*$^{f/+}$*Vav1*^{cre} and *Riok2*$^{+/+}$*Vav1*^{cre} mice (Extended Data Fig. 3a); however, long-term hematopoietic stem cells (LT-HSCs) were increased in the BM of aged *Riok2*$^{f/+}$*Vav1*^{cre} mice (Extended Data Fig. 3a). To further corroborate these data, we analyzed the capacity of *Riok2*-haploinsufficient cells in a competitive transplantation assay. Starting at 8 weeks after tamoxifen treatment to induce *Riok2* deletion, *Riok2*-haploinsufficient cells out-competed CD45.1$^+$ competitor cells, whereas *Ert2*^{cre} control cells had no competitive advantage (Extended Data Fig. 3b). Similarly to nontransplanted mice (Extended Data Fig. 3a), in competitive transplant experiments the frequency of *Riok2*-haploinsufficient LT-HSCs was significantly higher than *Riok2*-sufficient LT-HSCs in relation to competitor CD45.1$^+$ cells (Extended Data Fig. 3c). Thus, in addition to its effect on erythroid differentiation, *Riok2* haploinsufficiency increases myelopoiesis and affects early hematopoietic progenitor differentiation.

Reduced *Riok2* induces alarmins in erythroid precursors. To elucidate a mechanism for the erythroid differentiation defect observed in *Riok2*$^{f/+}$*Vav1*^{cre} mice, we performed quantitative proteomic analysis of purified erythroid precursors using mass spectrometry[30]. *Riok2* haploinsufficiency led to upregulation of 564 distinct proteins (adjusted *P* value <0.05) in erythroid precursors compared to those from *Vav1*^{cre} controls (Fig. 2a). Notably, *Riok2* haploinsufficiency resulted in downregulation of other ribosomal proteins, the loss of some of which (RPS5 and RPL11) has been implicated in driving anemias (Extended Data Fig. 4a). The alarmins including S100A8, S100A9, CAMP, NGP and others were the most highly upregulated proteins in our dataset and notably, correlated significantly with those observed upon haploinsufficiency of *Rps14* (ref. [10]), another component of the 40S ribosomal complex (Fig. 2b). Using the 26 upregulated proteins in the *Rps14*-haploinsufficient dataset as an 'Rps14 signature' (Supplementary Table 1), gene set enrichment analysis (GSEA) revealed a marked enrichment for the Rps14 signature in the *Riok2*-haploinsufficient dataset, suggesting a shared proteomic signature upon deletion of distinct

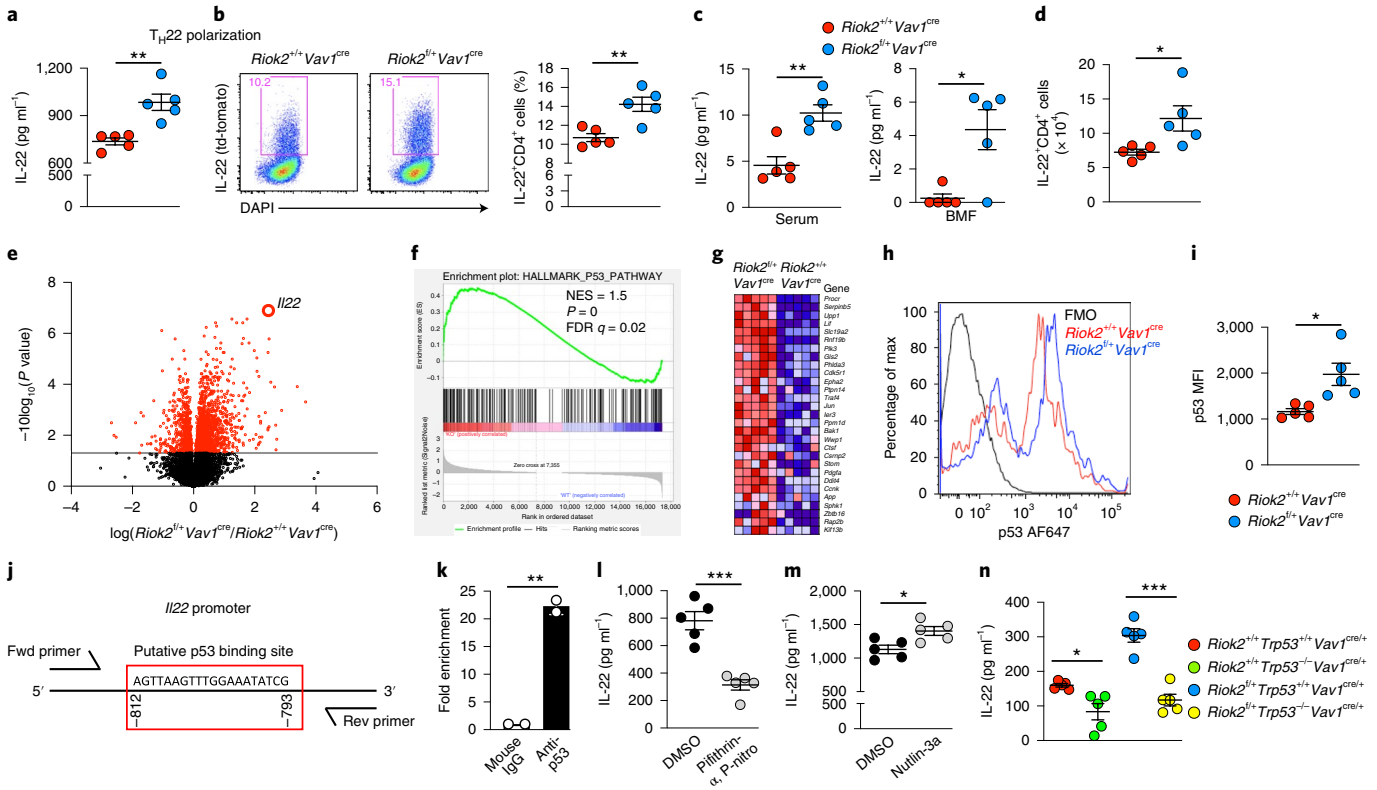

Fig. 3 | *Riok2* haploinsufficiency-driven p53 upregulation drives increased IL-22. a,**b**, Secreted IL-22 (**a**) and percentage of IL-22$^+$CD4$^+$ T cells (**b**) from in vitro polarized T$_H$22 cells from *Riok2*$^{f/+}$*Vav1*^{cre} mice and *Riok2*$^{+/+}$*Vav1*^{cre} controls ($n=5$ per group). **c**, IL-22 levels in serum (left) and BMF (right) in *Riok2*$^{f/+}$*Vav1*^{cre} mice and *Riok2*$^{+/+}$*Vav1*^{cre} controls ($n=5$ per group). **d**, Number of IL-22$^+$CD4$^+$ cells in the spleens of *Riok2*$^{f/+}$*Vav1*^{cre} mice and *Riok2*$^{+/+}$*Vav1*^{cre} controls ($n=5$ per group). **e**, Volcano plot showing transcriptomic changes in purified IL-22$^+$ cells from *Riok2*$^{f/+}$*Vav1*^{cre} mice in comparison to *Riok2*$^{+/+}$*Vav1*^{cre} controls ($n=5$ per group). **f**, GSEA showing activation of the p53 pathway in IL-22$^+$ cells from *Riok2*$^{f/+}$*Vav1*^{cre} mice in comparison to *Riok2*$^{+/+}$*Vav1*^{cre} controls. **g**, Snapshot of differentially expressed genes in the p53 pathway shown in **f** in *Riok2*$^{f/+}$*Vav1*^{cre} and *Riok2*$^{+/+}$*Vav1*^{cre} mice. **h**, Flow cytometry plot showing p53 expression in in vitro polarized T$_H$22 cells from *Riok2*$^{f/+}$*Vav1*^{cre} and *Riok2*$^{+/+}$*Vav1*^{cre} controls. **i**, Graphical representation of data shown in **h** ($n=5$ per group). **j**, Predicted p53 binding site in the *Il22* promoter region. **k**, ChIP showing p53 occupancy at the *Il22* promoter in T cells ($n=2$ independent experiments). **l**, Secreted IL-22 from WT T$_H$22 cells cultured in the presence or absence of p53 inhibitor, pifithrin-α, p-nitro (1 μM) ($n=5$ mice per group). **m**, Secreted IL-22 from WT T$_H$22 cells cultured in the presence or absence of p53 activator, nutlin-3 (100 nM) ($n=4$ mice per group). **n**, Secreted IL-22 from in vitro polarized T$_H$22 cells from the indicated strains ($n=5$ per group). Unpaired two-tailed Student's *t*-test (**a**–**d**,**i**,**k**–**m**) and one-way ANOVA with Tukey's correction for multiple comparison (**n**) used to calculate statistical significance. $^*P<0.05$, $^{**}P<0.01$, $^{***}P<0.001$. Data are shown as mean ± s.e.m and are representative of two (**c**,**d**,**h**,**i**,**k**–**n**) or three (**a**,**b**) independent experiments. Data in **k** are represented as mean ± s.d. and are pooled from two independent experiments.

ribosomal proteins (Fig. 2c). The increased expression of S100A8 and S100A9 in *Riok2*$^{f/+}$*Vav1*^{cre} mice was confirmed by flow cytometry and quantitative PCR with reverse transcription (qRT–PCR) (Extended Data Fig. 4b–e).

In *Riok2*$^{f/+}$*Vav1*^{cre} erythroid precursors cells, the upregulated proteins with the highest fold change (S100A8, S100A9, CAMP and NGP) are proteins with known immune functions such as antimicrobial defense. GSEA analysis of the proteomics data indicated a possible role for the immune system in driving the proteomic changes seen in *Riok2*-haploinsufficient erythroid precursors (Fig. 2d). An independent analysis of the Riok2 proteomics dataset using MetaCore pathway analysis software showed immune response as the top differentially regulated pathway in *Riok2*$^{f/+}$*Vav1*^{cre} mice (Fig. 2e). To assess whether *Riok2* haploinsufficiency leads to changes in immune cell function, we subjected naive T cells from *Riok2*$^{f/+}$*Vav1*^{cre} mice and *Riok2*$^{+/+}$*Vav1*^{cre} controls to in vitro polarization toward known CD4$^+$ helper T cell lineages (T$_H$1, T$_H$2, T$_H$17, T$_H$22) and regulatory T (T$_{reg}$) cells. Secretion of interferon (IFN)-γ, IL-2, IL-4, IL-5, IL-13, IL-17A and the frequency of Foxp3$^+$ T$_{reg}$ cells was similar between *Riok2*$^{f/+}$*Vav1*^{cre} and *Riok2*$^{+/+}$*Vav1*^{cre} T cells (Extended Data Fig. 5a–g). Notably, however, we observed an exclusive increase in IL-22 secretion from *Riok2*$^{f/+}$*Vav1*^{cre} naive T cells polarized toward the T$_H$22 cell lineage (Fig. 3a). The frequency of IL-22$^+$CD4$^+$ T cells was higher in *Riok2*$^{f/+}$*Vav1*^{cre} T$_H$22 cell cultures compared to *Vav1*^{cre} control T$_H$22 cell cultures (Fig. 3b). The concentration of IL-22 in the serum and BM fluid (BMF) of aged *Riok2*$^{f/+}$*Vav1*^{cre} mice was also significantly higher compared to age-matched *Vav1*^{cre} controls (Fig. 3c). Using known IL-22 target genes from the literature, we curated an 'IL-22 signature' (Supplementary Table 1) gene set, which showed a statistically significant enrichment in the *Riok2*-haploinsufficient proteomics dataset using GSEA (Fig. 2f), further suggesting that IL-22-induced inflammation is a contributing factor for *Riok2* haploinsufficiency-mediated ineffective erythropoiesis and anemia. Increased numbers of splenic IL-22$^+$CD4$^+$ T cell, natural killer T (NKT) cell and innate lymphoid cells (ILCs) were observed in aged *Riok2*$^{f/+}$*Vav1*^{cre} mice compared to *Riok2*$^{+/+}$*Vav1*^{cre} mice (Fig. 3d and Extended Data Fig. 5h,i). Notably, mild anemia was observed in mice lacking *Riok2* only in T cells (Extended Data Fig. 5k). Expression of IL-23, required for IL-22 production, was enhanced in *Riok2*-haploinsufficient dendritic cells (Extended Data Fig. 5j).

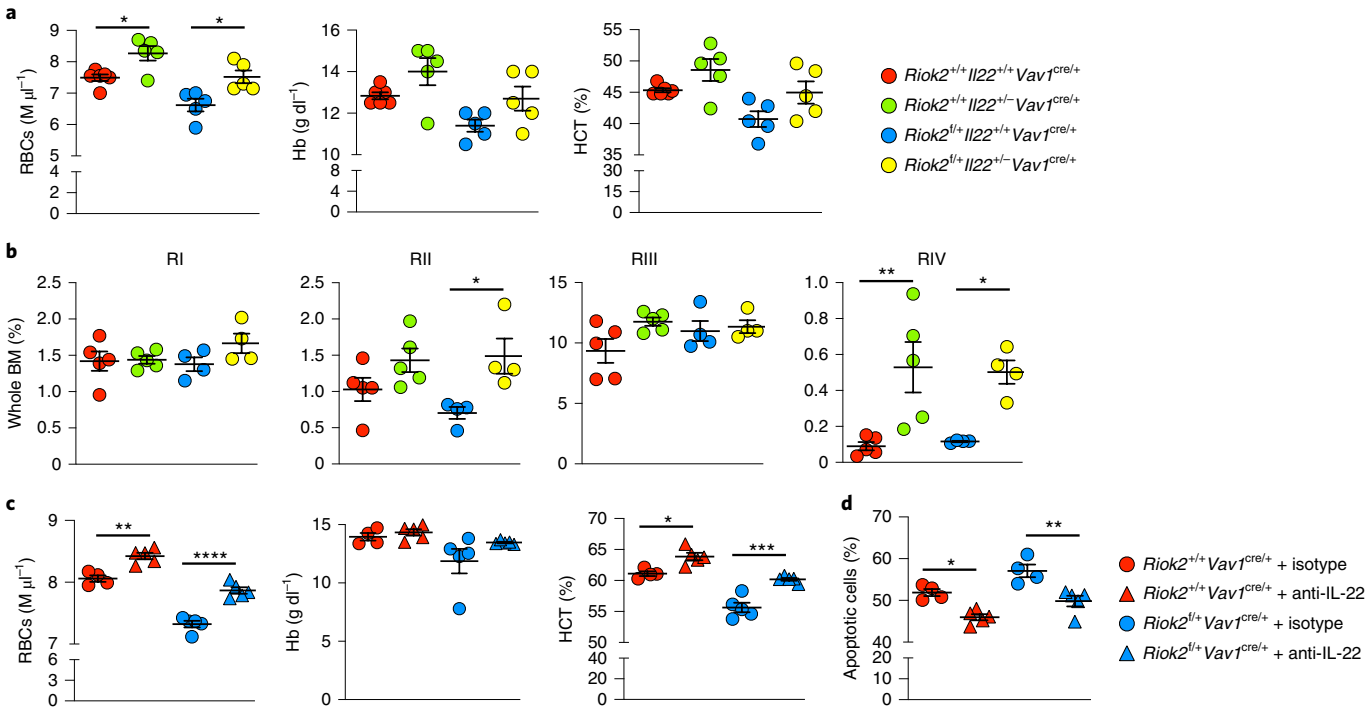

Fig. 4 | IL-22 neutralization alleviates stress-induced anemia in *Riok2*-sufficient and -haploinsufficient mice. a, PB RBC numbers, Hb and HCT in the indicated strains undergoing PhZ-induced stress erythropoiesis ($n = 6$, 5, 5 and 5 mice for *Riok2*$^{+/+}$*Il22*$^{+/+}$*Vav1*^{cre}, *Riok2*$^{+/+}$*Il22*$^{+/-}$*Vav1*^{cre}, *Riok2*$^{f/+}$*Il22*$^{+/+}$*Vav1*^{cre} and *Riok2*$^{f/+}$*Il22*$^{+/-}$*Vav1*^{cre}, respectively). **b**, Frequency of erythroid progenitor/precursor populations among viable BM cells in the indicated strains undergoing PhZ-induced stress erythropoiesis ($n = 4$–5 per group). **c**, PB RBC numbers, Hb and HCT in *Riok2*$^{f/+}$*Vav1*^{cre} mice and *Riok2*$^{+/+}$*Vav1*^{cre} controls undergoing PhZ-induced stress erythropoiesis treated with either an isotype control or anti-IL-22 antibody ($n = 4$–5 per group). **d**, Frequency of apoptotic erythroid precursors among viable BM cells in *Riok2*$^{f/+}$*Vav1*^{cre} mice and *Riok2*$^{+/+}$*Vav1*^{cre} controls undergoing PhZ-induced stress erythropoiesis treated with either an isotype control or anti-IL-22 antibody ($n = 4$, 5, 4 and 5 mice for isotype-treated *Riok2*$^{+/+}$*Vav1*^{cre}, anti-IL-22-treated *Riok2*$^{+/+}$*Vav1*^{cre}, isotype-treated *Riok2*$^{f/+}$*Vav1*^{cre} and anti-IL-22-treated *Riok2*$^{f/+}$*Vav1*^{cre} mice, respectively). One-way ANOVA with Tukey's correction for multiple comparison (**a**–**d**) was used to calculate statistical significance. $^{*}P < 0.05$, $^{**}P < 0.01$, $^{***}P < 0.001$, $^{****}P < 0.0001$. Data are shown as mean ± s.e.m and are representative of two (**c**,**d**) or three (**a**,**b**) independent experiments.

Rps14-haploinsufficient T_H22 cells also secreted elevated concentrations of IL-22 compared to *Vav1*^{cre} control T_H22 cells (Extended Data Fig. 5l). Mutation(s) in the gene adenomatosis polyposis coli (*Apc*), also found on human chromosome 5q, lead to anemia in addition to adenomas[31]. In vitro generated T_H22 cells from *Apc*^{Min} mice secreted elevated IL-22 levels compared to littermate controls (Extended Data Fig. 5m). In total, our analysis of three distinct heterozygous deletions of genes found on human chromosome 5q suggests that increased IL-22 is a generalized phenomenon observed upon heterozygous loss of genes found on chromosome 5q, leading to anemia.

p53 upregulation drives increased IL-22 secretion upon *Riok2* loss. To identify cell-intrinsic molecular mechanism(s) driving the increase in IL-22 secretion upon *Riok2* haploinsufficiency, we performed RNA-sequencing (RNA-seq) on in vitro polarized IL-22^{+} (T_H22) cells purified by flow cytometry from *Riok2*$^{+/+}$*Il22*$^{tdtomato/+}$*Vav1*^{cre} and *Riok2*$^{f/+}$*Il22*$^{tdtomato/+}$*Vav1*^{cre} mice (Fig. 3e). GSEA of the RNA-seq dataset identified activation of the p53 pathway in *Riok2*$^{f/+}$*Vav1*^{cre} mice (Fig. 3f,g). p53 increase in T_H22 cells from *Riok2*$^{f/+}$*Vav1*^{cre} mice was confirmed by flow cytometry (Fig. 3h,i). p53 upregulation was also observed in *Riok2*$^{f/+}$*Vav1*^{cre} erythroid precursors (Extended Data Fig. 3f,g). The p53 pathway is activated by decreased expression of ribosomal protein genes[5,10]; however, its involvement in IL-22 regulation is not known.

p53 is a transcription factor with well-defined consensus binding sites. To assess whether p53 drives *Il22* transcription, we analyzed the *Il22* promoter for potential p53 binding sites using LASAGNA algorithm and found putative p53 consensus binding sequences in the *Il22* promoter (Fig. 3j). Chromatin immunoprecipitation (ChIP) confirmed the presence of p53 on the *Il22* promoter (Fig. 3k). In line with the ChIP data, p53 inhibition by pifithrin-α, p-nitro decreased IL-22 concentrations, whereas p53 activation by nutlin-3 increased IL-22 from in vitro polarized WT T_H22 cells (Fig. 3l,m). Treatment with either pifithrin-α, p-nitro or nutlin-3 did not decrease cell viability (Extended Data Fig. 5n). Accordingly, genetic deletion of *Trp53* blunted the increase in IL-22 secretion observed upon *Riok2* haploinsufficiency (Fig. 3n). A significant decrease in IL-22 secretion was also observed upon *Trp53* deletion in Riok2-sufficient cells further suggesting a homeostatic role for p53 in controlling IL-22 production (Fig. 3n). Taken together, these data show that *Riok2* haploinsufficiency-mediated p53 upregulation drives increased IL-22 secretion in *Riok2*$^{f/+}$*Vav1*^{cre} mice.

IL-22 neutralization alleviates stress-induced anemia. Mice with compound genetic deletion of *Il22* on the *Riok2*-haploinsufficient background (*Riok2*$^{f/+}$*Il22*$^{+/-}$*Vav1*^{cre}) exhibited increased numbers of PB RBCs compared to IL-22-sufficient *Riok2*-haploinsufficient mice on day 7 after two treatments with 25 mg per kg phenylhydrazine treatment (Fig. 4a). Interestingly, we also saw an increase in PB RBCs in *Riok2*-sufficient mice heterozygous for *Il22* deletion (*Riok2*$^{+/+}$*Il22*$^{+/-}$*Vav1*^{cre}) compared to *Riok2*-sufficient IL-22 sufficient mice (*Riok2*$^{+/+}$*Il22*$^{+/+}$*Vav1*^{cre}). PB Hb and HCT also were increased in *Il22*-haploinsufficient mice, regardless of *Riok2*

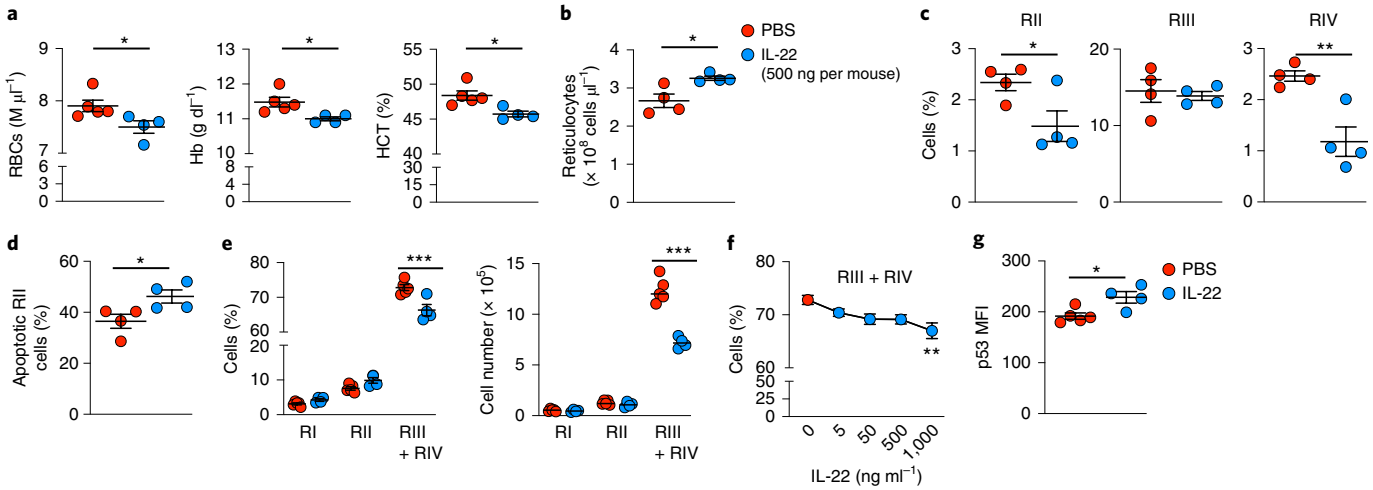

Fig. 5 | Recombinant IL-22 exacerbates PhZ-induced anemia in WT mice. a, PB RBC numbers, Hb and HCT in WT C57BL/6J mice administered PBS ($n=5$) or rIL-22 ($n=4$) and subsequently treated with PhZ ($n=4$–5 mice per group). **b**, PB reticulocytes in mice treated as in **a** ($n=4$ mice per group). **c**, Percentage of RII–RIV erythroid precursors in the BM of PBS- or rIL-22-treated C57BL/6J mice 7 d after PhZ administration ($n=4$ mice per group). **d**, Percentage of apoptotic RII erythroid precursors in mice treated as in **c** ($n=4$ mice per group). **e**,**f**, Effect of recombinant IL-22 (500 ng ml^{-1}) on the frequency (left) and cell number (right) in an in vitro erythropoiesis assay (**e**) and dose-dependent effect of recombinant IL-22 (**f**) ($n=5$ and 4 for PBS and IL-22 groups, respectively). **g**, p53 expression in in vitro erythropoiesis culture treated with rIL-22 or PBS ($n=5$ and 4 mice for PBS and IL-22 groups, respectively). Data are shown as mean ± s.e.m and are representative of three (**a**,**b**) or two (**c**–**g**) independent experiments. Unpaired two-tailed Student's *t*-test (**a**–**d**,**g**), multiple unpaired two-tailed Student's *t*-tests with Holm–Sidak method (**e**) and one-way ANOVA with Tukey's correction for multiple comparisons (**f**) were used to calculate statistical significance. *$P<0.05$, **$P<0.01$, ***$P<0.001$, ****$P<0.0001$.

background; however, this difference did not reach statistical significance (Fig. 4a). Next, we assessed whether the increase in PB RBCs in *Riok2*$^{f/+}$*Il22*$^{+/-}$*Vav1*^{cre} mice was due to increased erythropoiesis in the BM of these mice. We observed an increase in RII and RIV erythroid precursors in *Riok2*$^{f/+}$*Il22*$^{+/-}$*Vav1*^{cre} compared to *Riok2*$^{f/+}$*Il22*$^{+/+}$*Vav1*^{cre} mice (Fig. 4b and Extended Data Fig. 6a). Treatment of mice with a neutralizing IL-22 antibody in vivo, also reversed phenylhydrazine-induced anemia as evidenced by increase in PB RBCs and HCT in *Riok2*$^{f/+}$*Vav1*^{cre} mice as well as *Riok2*-sufficient (*Riok2*$^{+/+}$*Vav1*^{cre}) mice (Fig. 4c). Unexpectedly, IL-22 neutralization also reduced the frequency of apoptotic erythroid precursors in both *Riok2*-sufficient as well as *Riok2*$^{f/+}$*Vav1*^{cre} mice (Fig. 4d). These data indicate that IL-22 neutralization reverses anemia, at least in part, by reducing apoptosis of erythroid precursors. Recently, dampening IL-22 signaling in intestinal epithelial stem cells was shown to reduce apoptosis[32]. The effect of IL-22 deficiency (genetic as well as antibody-mediated) in alleviating anemia in genetically WT mice indicated a role for IL-22 in reversing anemia regardless of ribosomal haploinsufficiency. Accordingly, treatment of C57BL/6J mice undergoing phenylhydrazine-induced anemia with anti-IL-22 significantly increased PB RBCs, Hb and HCT compared to isotype antibody-treated mice (Extended Data Fig. 7b). This increase in PB RBCs could be attributed to the increased frequency of RIII and RIV erythroid precursors in the BM of mice treated with anti-IL-22 compared to isotype-administered controls (Extended Data Fig. 7c). Of note, PB RBCs, Hb and HCT did not differ in healthy, non-anemic WT mice injected with anti-IL-22 versus isotype-matched antibody (Extended Data Fig. 7a). Thus, we show here that IL-22 neutralization, either by genetic deletion or antibody blockade, alleviates stress-induced anemia in *Riok2*$^{f/+}$*Vav1*^{cre} as well as WT mice.

IL-22 worsens stress-induced anemia in wild-type mice. Phenylhydrazine administration to WT C57BL/6J mice treated intraperitoneally with recombinant IL-22 (rIL-22) led to decreased PB RBCs, Hb and HCT owing to decreased BM erythroid precursor cell frequency and number (Fig. 5a,c and Extended Data Fig. 6b). rIL-22 treatment led to increased apoptosis of erythroid precursors (Fig. 5d). This treatment also led to an increase in PB reticulocytes, an indication of increased erythropoiesis under stress (Fig. 5b). Recombinant IL-22 also dose-dependently decreased terminal erythropoiesis in an in vitro erythropoiesis assay (Fig. 5e,f). Notably, IL-22-mediated inhibition of in vitro erythropoiesis led to induction of p53 suggesting a feedback loop between IL-22 and p53 in driving dyserythropoiesis (Fig. 5g). Overall, these data show that exogenous recombinant IL-22 exacerbates stress-induced anemia in WT mice.

Erythroid precursors express IL-22RA1 receptors. IL-22 signals through a cell surface heterodimeric receptor composed of IL-10Rβ and IL-22RA1 (encoded by *Il22ra1*)[33]. IL-22RA1 expression has been reported to be restricted to cells of nonhematopoietic origin (for example, epithelial cells and mesenchymal cells). We discovered, however, that erythroid precursors in the BM also express IL-22RA1 (Fig. 6a and Extended Data Fig. 8a). Moreover, we observed that among BM hematopoietic progenitors, IL-22RA1-expressing cells were exclusively of the erythroid lineage (Extended Data Fig. 8b). Using a second IL-22RA1-specific antibody (targeting a different epitope than the antibody used in Fig. 4a), we confirmed the presence of IL-22RA1 on erythroid precursors (Extended Data Fig. 8c). *Il22ra1* mRNA expression was detected exclusively in erythroid precursors among all lineage-negative cells in the BM (Extended Data Fig. 8d).

Deletion of *Il22ra1* in *Riok2*-haploinsufficient mice (*Riok2*$^{f/+}$*Il22ra1*$^{f/f}$*Vav1*^{cre}) led to improvement in PB RBCs and HCT compared to IL-22RA1 sufficient *Riok2*-haploinsufficient mice (*Riok2*$^{f/+}$*Il22ra1*$^{+/+}$*Vav1*^{cre}) (Fig. 6b). This improvement could be attributed to the increase in RIII and RIV erythroid precursors in the BM of *Riok2*$^{f/+}$*Il22ra1*$^{f/f}$*Vav1*^{cre} mice (Fig. 6c and Extended Data Fig. 6c).

In accordance with the upregulation of p53 upon in vitro IL-22 stimulation in an in vitro erythropoiesis assay (Fig. 5g) and p53 upregulation in erythroid precursors upon *Riok2* haploinsufficiency (Extended Data Fig. 4f,g), we observed a synergistic effect of *Riok2* haploinsufficiency in IL-22-responsive (IL-22RA1^{+})

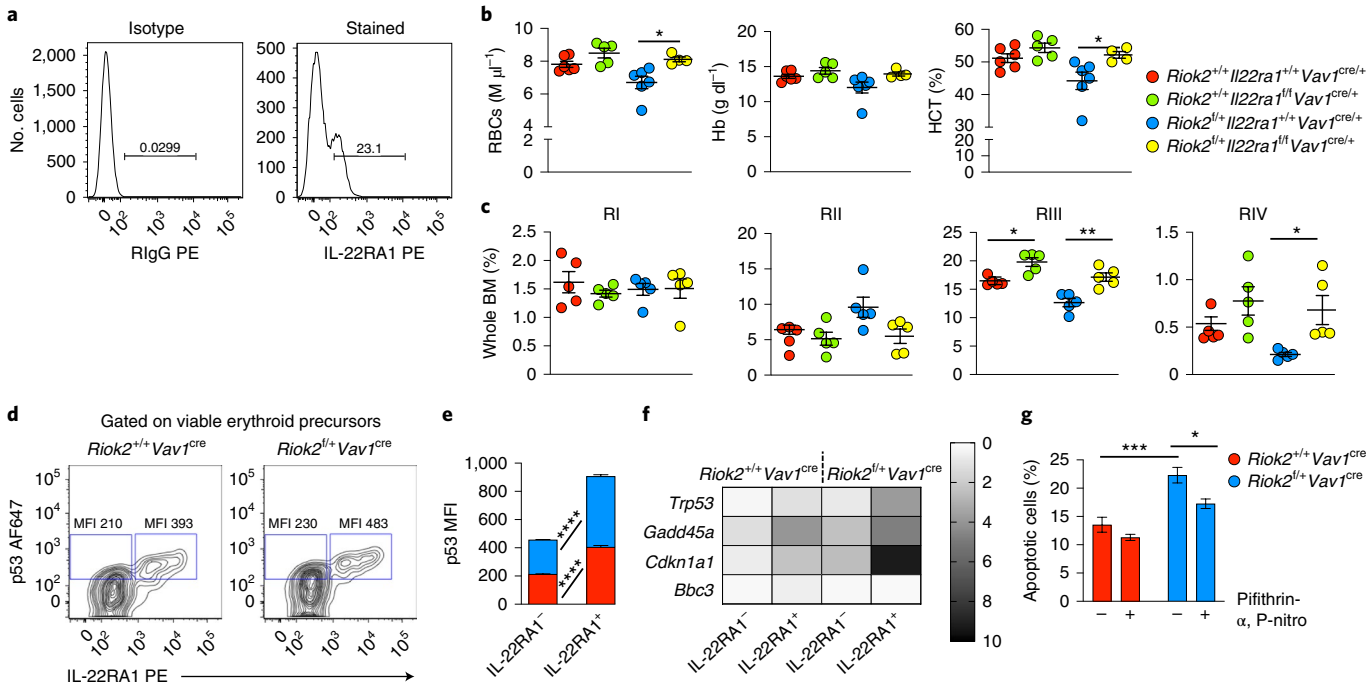

Fig. 6 | Genetic deletion of *Il22ra1* alleviates anemia in *Riok2*-haploinsufficient mice. a, IL-22RA1 expression on BM erythroid precursors in WT mice assessed by flow cytometry using antibody from Novus Biologicals targeting the extracellular domain of IL-22RA1. **b**, PB RBC numbers, Hb and HCT in the indicated strains undergoing PhZ-induced stress erythropoiesis ($n = 6$, 5, 6 and 4 mice for *Riok2*$^{+/+}$*Il22r1a*$^{+/+}$*Vav1*^{cre}, *Riok2*$^{+/+}$*Il22ra1*$^{f/f}$*Vav1*^{cre}, *Riok2*$^{f/+}$*Il22ra1*$^{+/+}$*Vav1*^{cre} and *Riok2*$^{f/+}$*Il22ra1*$^{f/f}$*Vav1*^{cre}, respectively). **c**, Frequency of erythroid progenitor/precursor populations among viable BM cells in the indicated strains undergoing PhZ-induced stress erythropoiesis ($n = 5$ per group). **d**, Flow cytometry plots showing p53 expression in IL-22RA1$^+$ and IL-22RA1$^-$ erythroid precursors in *Riok2*$^{f/+}$*Vav1*^{cre} mice and *Riok2*$^{+/+}$*Vav1*^{cre} controls ($n = 5$ per group). **e**, Graphical representation of data shown in **d**. **f**, Gene expression of *Trp53* (p53) and listed p53 target genes in IL-22RA1$^+$ and IL-22RA1$^-$ erythroid precursors from *Riok2*$^{f/+}$*Vav1*^{cre} and *Riok2*$^{+/+}$*Vav1*^{cre} mice assessed by qRT-PCR ($n = 3$ per group). **g**, Frequency of apoptotic cells (assessed by flow cytometry) with ($n = 4$) or without ($n = 5$) p53 inhibitor, pifithrin-α, p-nitro (1 μM), in an in vitro erythropoiesis assay using Lin$^-$ BM cells from *Riok2*$^{f/+}$*Vav1*^{cre} and *Riok2*$^{+/+}$*Vav1*^{cre} mice. Two-way ANOVA with Tukey's correction for multiple comparisons (**e**,**g**) and one-way ANOVA with Tukey's correction for multiple comparison (**b**,**c**) were used to calculate statistical significance. $^*P < 0.05$, $^{**}P < 0.01$, $^{***}P < 0.001$, $^{****}P < 0.0001$. Data are shown as mean ± s.e.m and are representative of two (**d**–**g**) or three (**a**–**c**) independent experiments.

erythroid precursors in *Riok2*$^{f/+}$*Vav1*^{cre} mice (Fig. 6d,e). p53 target genes such as *Gadd45a* and *Cdkn1a1* were also increased in IL-22RA1$^+$ *Riok2*-haploinsufficient erythroid precursors compared to IL-22RA1$^+$ *Riok2*-sufficient erythroid precursors (Fig. 6f). Given that rIL-22 induced apoptosis in erythroid precursors in vivo (Fig. 5d), we sought to determine whether *Riok2* haploinsufficiency-mediated p53 upregulation played an independent role in apoptosis induction. In an IL-22-free in vitro erythropoiesis assay, p53 inhibition by pifithrin-α, p-nitro inhibited the apoptosis induced by *Riok2* haploinsufficiency (Fig. 6g).

Erythroid cell-specific deletion of IL-22RA1 (using cre recombinase driven by the erythropoietin receptor (*Epor*) promoter) also increased numbers of PB RBCs and HCT (Fig. 7a) due to the increase in RIII and RIV erythroid precursors in the BM (Fig. 7b and Extended Data Fig. 6d). Additionally, rIL-22 failed to exacerbate phenylhydrazine-induced anemia in *Il22ra1*$^{f/f}$*Epor*^{cre} mice lacking the IL-22 receptor only on erythroid cells (Fig. 7c). These data reinforce our view that IL-22 signaling plays an important role in regulating erythroid development regardless of ribosomal haploinsufficiency. Thus, using three different approaches to neutralize IL-22 signaling, we demonstrate that IL-22 plays a critical role in controlling RBC production by directly regulating early stages of erythropoiesis.

IL-22 is increased in patients with del(5q) MDS. Next, we assessed whether IL-22 expression is increased in human disorders that display dyserythropoiesis due to ribosomal protein haploinsufficiencies. Given the localization of *RIOK2* on human chromosome 5, we focused on MDSs with 5q deletion and compared it to MDSs without 5q deletion and healthy controls. We observed a significant increase in IL-22 levels in the BMF of patients with del(5q) MDSs compared to BMF from healthy controls and patients with non-del(5q) MDSs (Fig. 8a). Notably, a strong negative correlation between cellular *RIOK2* messenger RNA expression and BMF IL-22 concentration was evident in the del(5q) MDS cohort (Fig. 8b), indicating that a decrease in *RIOK2* expression is associated with increased IL-22 expression. In our MDS cohort, S100A8 concentrations were found to be higher than healthy controls regardless of del(5q) status (Fig. 8c). However, IL-22 positively correlated with S100A8 concentrations only in the del(5q) MDS group (Fig. 8d). Of note, S100A8 concentrations were higher in BMF from patients with non-del(5q) MDS compared to those with del(5q) (Fig. 8c). These data suggest that the regulation of S100A8 expression may be IL-22-mediated in patients with del(5q) MDSs, but IL-22-independent in other subtypes of MDSs. In a second cohort of patients with MDSs, the frequency of CD4$^+$ T cells producing IL-22 (T_H22 cells) among freshly isolated peripheral blood mononuclear cells (PBMCs) was significantly higher in patients with MDSs with 5q deletion compared to healthy controls (Fig. 8e; cumulative data of representative flow plots shown in Extended Data Fig. 9a). Our independent analysis of a large-scale microarray sequencing dataset of CD34$^+$ cells from healthy controls and patients with del(5q) MDSs

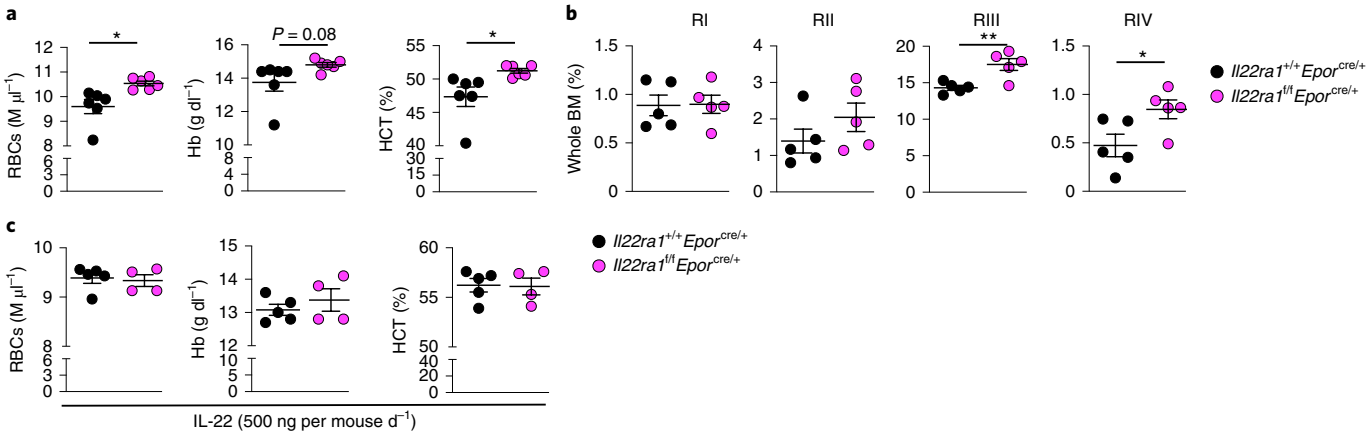

Fig. 7 | Erythroid-specific deletion of IL-22RA1 alleviates stress-induced anemia. a, PB RBC numbers, Hb and HCT in the indicated strains undergoing PhZ-induced stress erythropoiesis ($n = 6$ per group). **b**, Frequency of erythroid progenitor/precursor populations among viable BM cells in the indicated strains undergoing PhZ-induced stress erythropoiesis ($n = 5$ per group). **c**, PB RBC numbers, Hb and HCT in *Il22ra1*$^{+/+}$*Epor*^{cre} ($n = 5$) and *Il22ra1*$^{f/f}$*Epor*^{cre} ($n = 4$) mice administered rIL-22 and subsequently treated with PhZ ($n = 4$–5 mice per group). Unpaired two-tailed Student's *t*-test (**a**–**c**) used to calculate statistical significance. $^{*}P < 0.05$, $^{***}P < 0.001$. Data are shown as mean ± s.e.m and are representative of two (**a**–**c**) independent experiments.

and non-del(5q) MDSs showed that *RIOK2* mRNA was significantly decreased in the del(5q) MDS cohort (78% (37/47)). Additionally, expression of known IL-22 target genes such as *S100A10*, *S100A11*, *PTGS2*, *RAB7A* and *LCN2* was specifically increased in the del(5q) MDS cohort compared to both the healthy control and non-del(5q) groups (Extended Data Fig. 9b). Using differentially expressed proteins (adjusted *P* value <0.01) from the *Riok2*-haploinsufficient proteomics dataset as a reference set, GSEA of the CD34^{+} microarray dataset revealed significant enrichment scores (Extended Data Fig. 10a,b) further suggesting that the mouse model of *Riok2* haploinsufficiency faithfully recapitulates the molecular changes seen in patients with del(5q) MDSs.

High IL-22 in anemic patients with chronic kidney disease. Anemia is frequently observed in patients with chronic kidney disease (CKD) and is associated with poor outcomes. Anemia of CKD is resistant to erythropoiesis-stimulating agents in 10–20% of patients[34], suggesting that pathogenic mechanisms other than erythropoietin deficiency are at play. We found a significant increase in IL-22 concentration in the plasma of patients with CKD with secondary anemia compared to healthy controls and to patients with CKD without anemia (Fig. 8f). Plasma IL-22 concentration negatively correlated with hemoglobin in patients with CKD (Fig. 8g), suggesting a function for IL-22 in driving anemia in some patients with CKD.

Discussion

The overall conclusion of this study is that IL-22 signaling directly controls BM erythroid differentiation and that its neutralization is a potential therapeutic approach for anemias and MDSs. By exploring the function of a little-studied atypical kinase Riok2 in mammalian biology, we identified the erythroid precursors as a new target for IL-22 action via IL-22RA1. We further identified IL-22 as a disease biomarker for the del(5q) subtype of MDSs and last, we identified IL-22 signaling blockade as a potential therapeutic for stress-induced anemias irrespective of genetic background. Notably, we also detected elevated levels of IL-22 in patients with anemia secondary to CKD, suggesting that IL-22 signaling blockade may be therapeutic in reversing anemia in a much wider patient population.

Del(5q), either isolated or accompanied by additional cytogenetic abnormalities, is the most commonly detected chromosomal abnormality in MDSs, reported in 10–15% of patients and enriched in therapy-related MDSs. The severe anemia in patients with MDSs with isolated del(5q) has been linked to haploinsufficiency of ribosomal proteins such as RPS14 (ref. [10]) and RPS19 (ref. [5]). While much research has focused on the effect of such gene deletions or mutations in hematopoietic stem cells and lineage-committed progenitors, the immunobiology underlying this MDS subtype has remained largely unexplored, thus impeding the development of immune-targeted therapies. With the exception of the tumor necrosis factor-α inhibitor etanercept[35], which proved to be ineffective, the only other therapy against immune cell-derived cytokines is luspatercept[36], a recombinant fusion protein derived from human activin receptor type IIb[37], which has just been approved for use in anemia in lower risk patients with MDSs. Here, we identify two critical and independent functions of an understudied atypical kinase, RIOK2, that synergize to induce dyserythropoiesis and anemia. One effect of *Riok2* loss in erythroid precursors is an intrinsic block in erythroid differentiation owing to its indispensable role in the maturation of the pre-40S ribosomal complex, leading to increased apoptosis and cell cycle arrest. The second effect of *Riok2* loss is the induction of the erythropoiesis-suppressive cytokine IL-22 in T cells, which then directly acts on the IL-22RA1 on erythroid precursors (Extended Data Fig. 10c). While IL-22RA1 is known to be widely expressed on epithelial cells and hepatocytes, its expression has also been recently reported on specialized cells such as retinal Müller glial cells[38] and now described here, on erythroid precursors. Our data reveal a new molecular link between haploinsufficiency of a ribosomal protein and induction of erythropoiesis-suppressive cytokine IL-22. While IL-22 has been shown to modulate RBC production by controlling the expression of iron-chelating proteins such as hepcidin[39] and haptoglobin[40], we have uncovered a new role for IL-22 in directly binding to the previously unknown IL-22R on erythroid precursors leading to their apoptosis. Diminished expression of ribosomal proteins has been shown to increase p53 levels. We show here that *Riok2* haploinsufficiency leads to p53 upregulation in T cells, which drives the increase in IL-22 secretion. Additionally, we also show that IL-22-responsive erythroid precursors express elevated p53, further suggesting a role for p53 downstream of IL-22 signaling in driving dyserythropoiesis. Using banked and fresh del(5q) MDSs and samples from patients with CKD, we also show that IL-22 is elevated in these human diseases.

The role of inflammatory cytokines in directly regulating various aspects of BM hematopoiesis in steady-state and diseased conditions is increasingly being recognized[41–43]. IL-22 is known to play a pathogenic role in some autoimmune diseases[44,45]. Interestingly,

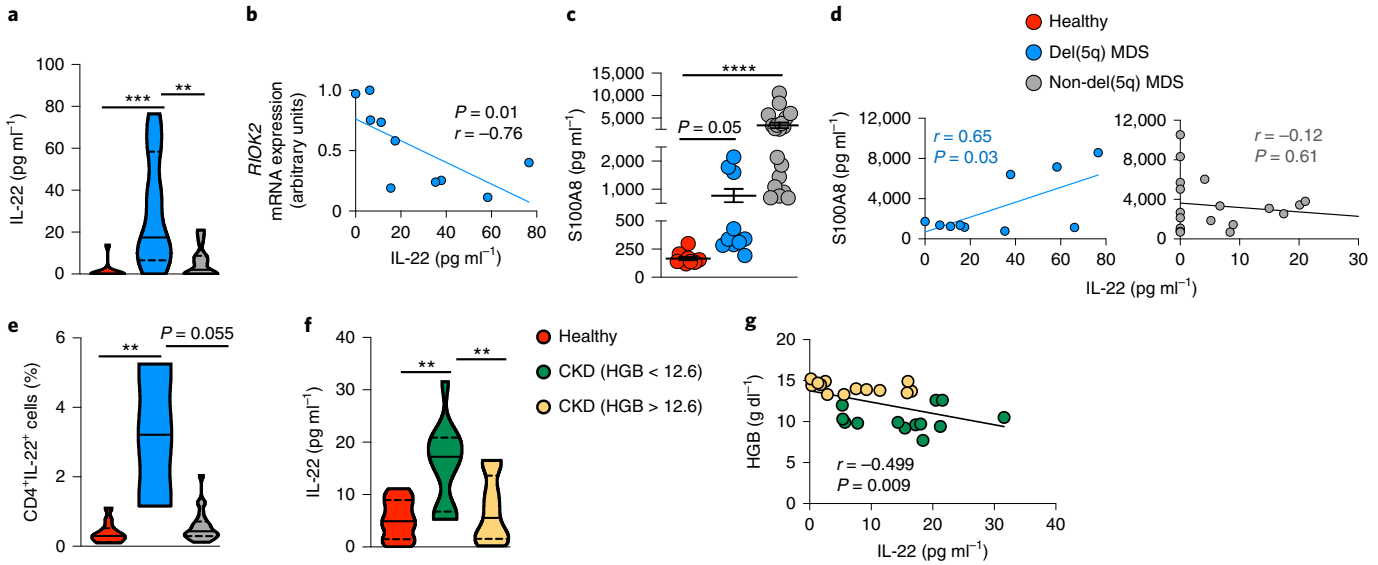

Fig. 8 | Patients with MDSs exhibit increased IL-22 levels and an IL-22-associated signature. a, IL-22 concentration in the BM fluid of healthy controls ($n=12$) and patients with del(5q) MDSs ($n=11$) and non-del(5q) MDSs ($n=22$). **b**, Correlation between *RIOK2* mRNA and BM IL-22 concentration in the del(5q) cohort shown in **a** ($n=10$). **c**, S100A8 concentration in the samples shown in **a** ($n=11$, 10 and 19 for healthy controls, del(5q) MDSs and non-del(5q) MDSs, respectively). **d**, Correlation between IL-22 concentration and S100A8 concentration in BM fluid of del(5q) (left, $n=10$) and non-del(5q) (right, n=19) samples. **e**, Frequency of IL-22-producing CD4$^+$ T cells in the PB of healthy controls ($n=11$) and patients with del(5q) ($n=3$) and non-del(5q) ($n=24$) MDSs. **f**, Plasma IL-22 concentration in healthy controls ($n=10$) and patients with CKD with ($n=13$) or without ($n=13$) secondary anemia. **g**, Correlation between plasma IL-22 concentration and Hb in patients with CKD with ($n=13$) or without ($n=13$) anemia. Kruskal–Wallis test with Dunn's correction for multiple comparisons (**a**–**c**,**e**) and a one-way ANOVA with Tukey's correction for multiple comparisons (**f**) were used to calculate statistical significance. Pearson correlation coefficient (**b**,**d**,**g**) was used to calculate statistical significance and correlation coefficients. $^{**}P<0.01$, $^{***}P<0.001$, $^{****}P<0.0001$. Data are shown as mean ± s.e.m (**c**). Solid lines represent median and dashed lines represent quartiles (**a**,**e**,**f**).

autoimmune diseases such as colitis, Behçet's disease and arthritis are common in patients with MDSs, with features of autoimmunity observed in up to 10% of patients[46]. It is intriguing to hypothesize that IL-22 may account both for the onset of MDSs and autoimmunity in this subset of patients. Studies have reported that in patients with coexistence of MDSs and autoimmunity, treatment for one can alleviate the symptoms of the other[47,48]. Low-level exposure to benzene, a hydrocarbon, has been associated with an increased risk of MDSs[49]. Hydrocarbons are known ligands for aryl hydrocarbon receptor (AHR), the transcription factor that controls IL-22 production in T cells. Stemregenin 1, an AHR antagonist, was shown to promote the ex vivo expansion of human hematopoietic stem cells, with the highest fold expansion seen in the erythroid lineage[50]. Overall, these observations suggest that inhibition of the AHR–IL-22 axis may be an attractive approach for treating RBC disorders that arise from dyserythropoiesis.

Further, we provide evidence that neutralization of IL-22 signaling may be effective not only in the treatment of MDSs and other stress-induced anemias, but also in the anemia of chronic diseases such as CKD, which are very much in need of new therapeutic approaches. With currently approved MDS therapies (lenalidomide and other hypomethylating agents, erythropoiesis-stimulating agents), the survival time of patients with MDSs after diagnosis is only 2.5–3 years. Patients also develop resistance to these therapies, thus intensifying the need for additional therapeutic modalities. IL-22-based therapies could be used in conjunction with already existing therapeutics or after first-line therapies have failed due to acquisition of resistance.

Online content

Any methods, additional references, Nature Research reporting summaries, source data, extended data, supplementary information, acknowledgements, peer review information; details of author contributions and competing interests; and statements of data and code availability are available at https://doi.org/10.1038/s41590-021-00895-4.

Received: 10 August 2020; Accepted: 3 February 2021;
Published online: 22 March 2021

References

1. Giagounidis, A. A., Germing, U. & Aul, C. Biological and prognostic significance of chromosome 5q deletions in myeloid malignancies. *Clin. Cancer Res.* **12**, 5–10 (2006).
2. Haase, D. et al. New insights into the prognostic impact of the karyotype in MDS and correlation with subtypes: evidence from a core dataset of 2124 patients. *Blood* **110**, 4385–4395 (2007).
3. Hofmann, W. K., Lubbert, M., Hoelzer, D. & Phillip Koeffler, H. Myelodysplastic syndromes. *Hematol. J.* **5**, 1–8 (2004).
4. Sole, F. et al. Incidence, characterization and prognostic significance of chromosomal abnormalities in 640 patients with primary myelodysplastic syndromes. Grupo Cooperativo Espanol de Citogenetica Hematologica. *Br. J. Haematol.* **108**, 346–356 (2000).
5. Dutt, S. et al. Haploinsufficiency for ribosomal protein genes causes selective activation of p53 in human erythroid progenitor cells. *Blood* **117**, 2567–2576 (2011).
6. Ebert, B. L. et al. Identification of RPS14 as a 5q- syndrome gene by RNA interference screen. *Nature* **451**, 335–339 (2008).
7. Kumar, M. S. et al. Coordinate loss of a microRNA and protein-coding gene cooperate in the pathogenesis of 5q- syndrome. *Blood* **118**, 4666–4673 (2011).
8. Ribezzo, F. et al. Rps14, Csnk1a1 and miRNA145/miRNA146a deficiency cooperate in the clinical phenotype and activation of the innate immune system in the 5q- syndrome. *Leukemia* **33**, 1759–1772 (2019).
9. Schneider, R. K. et al. Role of casein kinase 1A1 in the biology and targeted therapy of del(5q) MDS. *Cancer Cell* **26**, 509–520 (2014).
10. Schneider, R. K. et al. Rps14 haploinsufficiency causes a block in erythroid differentiation mediated by S100A8 and S100A9. *Nat. Med.* **22**, 288–297 (2016).
11. Zemp, I. et al. Distinct cytoplasmic maturation steps of 40S ribosomal subunit precursors require hRio2. *J. Cell Biol.* **185**, 1167–1180 (2009).

12. Muto, T. et al. Adaptive response to inflammation contributes to sustained myelopoiesis and confers a competitive advantage in myelodysplastic syndrome HSCs. *Nat. Immunol.* **21**, 535–545 (2020).
13. Smith, M. A. et al. U2AF1 mutations induce oncogenic IRAK4 isoforms and activate innate immune pathways in myeloid malignancies. *Nat. Cell Biol.* **21**, 640–650 (2019).
14. Starczynowski, D. T. & Karsan, A. Innate immune signaling in the myelodysplastic syndromes. *Hematol. Oncol. Clin. North Am.* **24**, 343–359 (2010).
15. Yang, L., Qian, Y., Eksioglu, E., Epling-Burnette, P. K. & Wei, S. The inflammatory microenvironment in MDS. *Cell. Mol. Life Sci.* **72**, 1959–1966 (2015).
16. Allampallam, K. et al. Measurement of mRNA expression for a variety of cytokines and its receptors in bone marrows of patients with myelodysplastic syndromes. *Anticancer Res.* **19**, 5323–5328 (1999).
17. Schipperus, M. R. et al. Interleukin-6 and interleukin-1 enhancement of GM-CSF-dependent proliferation of haematopoietic progenitor cells in myelodysplastic syndromes. *Br. J. Haematol.* **77**, 515–522 (1991).
18. Shao, L. L. et al. T_H22 cells as well as T_H17 cells expand differentially in patients with early-stage and late-stage myelodysplastic syndrome. *PLoS ONE* **7**, e51339 (2012).
19. Verhoef, G. E. et al. Measurement of serum cytokine levels in patients with myelodysplastic syndromes. *Leukemia* **6**, 1268–1272 (1992).
20. Starczynowski, D. T. & Karsan, A. Deregulation of innate immune signaling in myelodysplastic syndromes is associated with deletion of chromosome arm 5q. *Cell Cycle* **9**, 855–856 (2010).
21. Means, R. T. Jr. Pathogenesis of the anemia of chronic disease: a cytokine-mediated anemia. *Stem Cells* **13**, 32–37 (1995).
22. Song, M. et al. IRE1α-XBP1 controls T cell function in ovarian cancer by regulating mitochondrial activity. *Nature* **562**, 423–428 (2018).
23. Ferreira-Cerca, S. et al. ATPase-dependent role of the atypical kinase Rio2 on the evolving pre-40S ribosomal subunit. *Nat. Struct. Mol. Biol.* **19**, 1316–1323 (2012).
24. Royer-Pokora, B. et al. Delineation by molecular cytogenetics of 5q deletion breakpoints in myelodyplastic syndromes and acute myeloid leukemia. *Cancer Genet. Cytogenet.* **167**, 66–69 (2006).
25. Tang, G. et al. Isolated del(5q) in patients following therapies for various malignancies may not all be clinically significant. *Am. J. Clin. Pathol.* **144**, 78–86 (2015).
26. Boultwood, J. et al. Narrowing and genomic annotation of the commonly deleted region of the 5q- syndrome. *Blood* **99**, 4638–4641 (2002).
27. Lai, F. et al. Transcript map and comparative analysis of the 1.5-Mb commonly deleted segment of human 5q31 in malignant myeloid diseases with a del(5q). *Genomics* **71**, 235–245 (2001).
28. Seita, J. et al. Gene Expression Commons: an open platform for absolute gene expression profiling. *PLoS ONE* **7**, e40321 (2012).
29. Khajuria, R. K. et al. Ribosome levels selectively regulate translation and lineage commitment in human hematopoiesis. *Cell* **173**, 90–103 (2018).
30. Myers, S. A. et al. Streamlined protocol for deep proteomic profiling of FAC-sorted cells and its application to freshly isolated murine immune cells. *Mol. Cell. Proteom.* **18**, 995–1009 (2019).
31. Su, L. K. et al. Multiple intestinal neoplasia caused by a mutation in the murine homolog of the APC gene. *Science* **256**, 668–670 (1992).
32. Gronke, K. et al. Interleukin-22 protects intestinal stem cells against genotoxic stress. *Nature* **566**, 249–253 (2019).
33. Kotenko, S. V. et al. Identification of the functional interleukin-22 (IL-22) receptor complex: the IL-10R2 chain (IL-10Rβ) is a common chain of both the IL-10 and IL-22 (IL-10-related T cell-derived inducible factor, IL-TIF) receptor complexes. *J. Biol. Chem.* **276**, 2725–2732 (2001).
34. KDOQI & National Kidney Foundation. KDOQI clinical practice guidelines and clinical practice recommendations for anemia in chronic kidney disease. Am. J. Kidney Dis. 47, S11–S145 (2006).
35. Maciejewski, J. P. et al. A pilot study of the recombinant soluble human tumour necrosis factor receptor (p75)-Fc fusion protein in patients with myelodysplastic syndrome. *Br. J. Haematol.* **117**, 119–126 (2002).
36. Fenaux, P. et al. Luspatercept in patients with lower-risk myelodysplastic syndromes. *N. Engl. J. Med.* **382**, 140–151 (2020).
37. Suragani, R. N. et al. Transforming growth factor-β superfamily ligand trap ACE-536 corrects anemia by promoting late-stage erythropoiesis. *Nat. Med.* **20**, 408–414 (2014).
38. Mattapallil, M. J. et al. Interleukin 22 ameliorates neuropathology and protects from central nervous system autoimmunity. *J. Autoimmun.* **102**, 65–76 (2019).
39. Smith, C. L. et al. IL-22 regulates iron availability in vivo through the induction of hepcidin. *J. Immunol.* **191**, 1845–1855 (2013).
40. Sakamoto, K. et al. IL-22 controls iron-dependent nutritional immunity against systemic bacterial infections. *Sci. Immunol.* **2**, eaai8371 (2017).
41. Pietras, E. M. et al. Chronic interleukin-1 exposure drives haematopoietic stem cells towards precocious myeloid differentiation at the expense of self-renewal. *Nat. Cell Biol.* **18**, 607–618 (2016).
42. Yamashita, M. & Passegue, E. TNF-α coordinates hematopoietic stem cell survival and myeloid regeneration. *Cell Stem Cell* **25**, 357–372 e357 (2019).
43. Zhang, T. Y. et al. IL-6 blockade reverses bone marrow failure induced by human acute myeloid leukemia. *Sci. Transl. Med.* **12**, eaax5104 (2020).
44. Cai, T. et al. Increased expression of IL-22 is associated with disease activity in Behcet's disease. *PLoS ONE* **8**, e59009 (2013).
45. Yamamoto-Furusho, J. K. et al. Colonic epithelial upregulation of interleukin 22 (IL-22) in patients with ulcerative colitis. *Inflamm. Bowel Dis.* **16**, 1823 (2010).
46. Lee, S. J. et al. Certain autoimmune manifestations are associated with distinctive karyotypes and outcomes in patients with myelodysplastic syndrome: a retrospective cohort study. *Medicine (Baltimore)* **95**, e3091 (2016).
47. Fozza, C., La Nasa, G. & Caocci, G. The Yin and Yang of myelodysplastic syndromes and autoimmunity: The paradox of autoimmune disorders responding to therapies specific for MDS. *Crit. Rev. Oncol. Hematol.* **142**, 51–57 (2019).
48. Wolach, O. & Stone, R. Autoimmunity and Inflammation in myelodysplastic syndromes. *Acta Haematol.* **136**, 108–117 (2016).
49. Schnatter, A. R., Glass, D. C., Tang, G., Irons, R. D. & Rushton, L. Myelodysplastic syndrome and benzene exposure among petroleum workers: an international pooled analysis. *J. Natl Cancer Inst.* **104**, 1724–1737 (2012).
50. Boitano, A. E. et al. Aryl hydrocarbon receptor antagonists promote the expansion of human hematopoietic stem cells. *Science* **329**, 1345–1348 (2010).

Methods

Human samples and processing. Samples from patients with MDSs and CKD were collected under institutional review board-approved protocols at Dana-Farber Cancer Institute (DFCI) and Brigham and Women's Hospital, respectively. All samples were de-identified at the time of inclusion in the study. All patients provided informed consent and data collection was performed in accordance with the Declaration of Helsinki.

PBMCs from EDTA-treated whole blood were isolated using density gradient centrifugation. PBMCs were then incubated in RPMI with 10% FBS and Cell Activation Cocktail (Tonbo Biosciences) for 4 h and then processed for flow cytometry as described below. Relevant clinical information of MDS samples is provided in Supplementary Tables. Adult CKD plasma samples were stored at −80 °C until further use. Relevant clinical information of CKD samples is provided in Supplementary Table 3.

Generation of *Riok2* floxed mice. *Riok2*$^{f/f}$ mice were generated using frozen sperm obtained from Mutant Mouse Resource and Research Centers (*Riok2*$^{tm1a(KOMP)Wtsi}$)[51]. In brief, a floxed *Riok2* allele was created by inserting an FRT-flanked IRES-LacZ-*neo*^{r} cassette into intron 4 of the *Riok2* gene. *Lox*P sites were inserted to flank exons 5 and 6. After germline transmission, the FRT cassette was removed by crossing to FLPe deleter mice[52] and resulting floxed mice were bred with individual *cre* driver strains to create conditional *Riok2*-deleted mice (Extended Data Fig. 1a). Genotyping (Extended Data Fig. 1c) was carried out using the following primers:

Forward primer: 5′ GCATCAGTGATTTACAGACTAAAATGCC 3′
Reverse primer 1: 5′ GCTCTTACCCACTGAGTCATCTCACC 3′
Reverse primer 2: 5′ CCCAGACTCCTTCTTGAAGTTCTGC 3′

Mice. WT C57BL/6J mice (stock no. 000664), *Vav*-icre mice (stock no. 008610), R26-CreErt2 mice (stock no. 008463), *Il22ra1*-floxed (stock no. 031003), CD45.1 C57BL/6J mice (stock no. 002014), *Trp53*$^{-/-}$(stock no. 002101), *Cd4*-cre (stock no. 022071) and *Apc*^{Min} (stock no. 002020) mice were purchased from the Jackson Laboratory. *Il22*$^{-/-}$ mice were provided by R. Caspi (National Institutes of Health (NIH)) with permission from Genentech. *Epor*-cre[53] mice were a gift from U. Klingmüller (Deutsches Krebsforschungszentrum). *Il22*-tdtomato (Catch-22)[54] mice were a gift from R. Locksley (University of California San Francisco). *Rps14*-floxed mice[10] were a gift from B. Ebert (DFCI). Mice were housed in the Animal Research Facility at DFCI under ambient temperature and humidity with 12-h light/12-h dark cycle. Animal procedures and treatments were in compliance with the guidelines set forth by the Institutional Animal Care and Use Committee at DFCI. Age- and sex-matched mice were used within experiments.

Competitive BM transplantation. Overall, 2×10^6 freshly isolated BM cells from CD45.2$^+$ *Riok2*$^{f/+}$*Ert2*^{cre} or *Riok*$^{+/+}$*Ert2*^{cre} mice were transplanted in competition with 2×10^6 freshly isolated CD45.1$^+$ WT BM cells via retro-orbital injection into lethally irradiated 8–10-week-old CD45.1$^+$ WT recipient mice. The donor cell chimerism was determined in PB 4 weeks after transplantation before excision of *Riok2* was induced by tamoxifen injection as well as every 4–8 weeks as indicated. Tamoxifen (75 mg per kg) (Cayman Chemical, cat. no. 13258) was administered for 5 consecutive days.

Flow cytometry and cell isolation. Whole BM cells were isolated by crushing hind leg bones (femur and tibia) with mortar and pestle in staining buffer (PBS, Corning) supplemented with 2% heat-inactivated FBS (Atlanta Biologicals) and EDTA (GIBCO). Whole BM was lysed with 1× PharmLyse (BD Biosciences) for 90 s and the reaction was terminated by adding an excess of staining buffer. Cells were labeled with fluorochrome-conjugated antibodies in staining buffer for 30 min at 4 °C. For flow cytometric analysis, cells were incubated with combinations of fluorochrome-conjugated antibodies to the following cell surface markers: CD3 (17A2, 1:500 dilution), CD5 (53–7.3, 1:500 dilution), CD11b (M1/70, 1:500 dilution), Gr1 (RB6–8C5, 1:500 dilution), B220 (RA3–6B2, 1:500 dilution), Ter119 (TER119, 1:500 dilution), CD71 (C2, 1:500 dilution), c-kit (2B8, 1:500 dilution), Sca-1 (D7, 1:500 dilution), CD16/32 (93, 1:500 dilution), CD150 (TC15–12F12.2, 1:150 dilution) and CD48 (HM48-1, 1:500 dilution). For sorting of lineage-negative cells, lineage markers included CD3, CD5, CD11b, Gr1 and Ter119. For sorting erythroid progenitor cells, the lineage cocktail did not include Ter119. All reagents were acquired from BD Biosciences, Thermo Fisher Scientific, Novus Biologicals, Tonbo Biosciences or BioLegend. Identification of apoptotic cells was carried out using the Annexin V Apoptosis Detection kit (BioLegend). Intracytoplasmic and intranuclear staining was performed using Foxp3/Transcription Factor Staining kit (Thermo Fisher Scientific) or 0.1% saponin in PBS supplemented with 3% FBS. For staining performed with AF647 p53 antibody (Cell Signaling Technology, 1:50), cells were permeabilized with 90% ice-cold methanol. To increase sorting efficiency, whole BM samples were lineage-depleted using magnetic microbeads (Miltenyi Biotec) and AutoMACS Pro magnetic separator (Miltenyi Biotec). Cell sorting was performed on a FACS Aria flow cytometer (BD Biosciences), data acquisition was performed on a BD Fortessa X-20 instrument equipped with five lasers (BD Biosciences) employing FACSDiva software. Data were analyzed by FlowJo (Tree Star) v.9 software. Flow analyses were performed on viable cells by exclusion of dead cells using either DAPI or a fixable viability dye (Tonbo Biosciences). Gating for early and committed hematopoietic progenitors was performed as described elsewhere[55]. ILCs and NKT cells were identified as Lin$^-$ CD45$^+$CD90$^+$CD12$^+$ and CD3ε$^+$NK1.1$^+$, respectively.

Complete blood count. Mice were bled via the submandibular facial vein to collect blood in EDTA-coated tubes (BD Microtainer Capillary Blood Collector, BD 365974). Complete blood counts were obtained using the HemaVet CBC Analyzer (Drew Scientific) or Advia 120 (Siemens) instruments.

In vivo measurement of protein synthesis. A total of 100 µl of a 20 mM solution of O-Propargyl-Puromycin (OP-Puro; BioMol) was injected intraperitoneally in mice and mice were then rested for 1 h. Mice injected with PBS were used as controls. BM was collected after 1 h and stained with antibodies against cell surface markers, washed to remove excess unbound antibodies, fixed in 1% paraformaldehyde and permeabilized in PBS with 3% FBS and 0.1% saponin. The azide-alkyne cyclo-addition was performed using the Click-iT Cell Reaction Buffer kit (Thermo Fisher Scientific) and azide conjugated to Alexa Fluor 647 (Thermo Fisher Scientific) at 5 µM final concentration for 30 min. Cells were washed twice and analyzed by flow cytometry. 'Relative rate of protein synthesis' was calculated by normalizing OP-Puro signals to whole BM after subtracting autofluorescence.

Methylcellulose assay. The 250–500 BM Lin$^-$c-kit$^+$Sca-1$^+$ cells were flow sorted and plated in semi-solid methylcellulose culture medium (M3534, StemCell Technologies) and incubated at 37 °C in a humidified atmosphere for 7–10 d. At the end of the incubation period, each well was triturated with staining buffer to collect cells and then processed for flow cytometry as described above. Enumeration of colonies in MethoCult medium was performed with a StemVision instrument (StemCell Technologies).

Phenylhydrazine treatment. PhZ was purchased from Sigma and injected intraperitoneally on 2 consecutive days (days 0 and 1) at a dose of 25 mg per kg (sublethal model) or 35 mg per kg (lethal model). PB was collected 3–4 d before the start of treatment and at day 4, 7 and 11. PhZ treatment experiments were carried out in 8–12-week-old mice.

T cell polarization. Single-cell suspensions of mouse spleens were prepared by pressing tissue through a 70-µm cell strainer followed by RBC lysis using PharmLyse. Total splenic CD4$^+$ T cells were isolated using CD4$^+$ T cell isolation kit (Miltenyi Biotec). Enriched CD4$^+$ T cells were then incubated with fluorochrome-conjugated antibodies to CD4, CD8, CD25, CD62L and CD44 to purify naive CD4$^+$ T cells using FACS. In the presence of 1 µg ml^{-1} plate-bound anti-CD3ε and soluble 1 µg ml^{-1} anti-CD28, T cell polarizations were carried out in IMDM supplemented with 10% FBS, 2 mM L-glutamine, 100 mg ml^{-1} penicillin-streptomycin, HEPES (pH 7.2–7.6), nonessential amino acids, 100 µM β-mercaptoethanol (BME) and sodium pyruvate as follows: T_H1 (20 ng ml^{-1} IL-12 and 10 µg ml^{-1} anti-IL-4); T_H2 (20 ng ml^{-1} IL-4 and 10 µg ml^{-1} anti-IFN-γ); T_H17 (30 ng ml^{-1} IL-6, 20 ng ml^{-1} IL-23, 20 ng ml^{-1} IL-1β, 10 µg ml^{-1} anti-IL-4 and 10 µg ml^{-1} anti-IFN-γ); T_{reg} cells (1 ng ml^{-1} TGF-β, 10 µg ml^{-1} anti-IL-4 and 10 µg ml^{-1} anti-IFN-γ) and T_H22 (30 ng ml^{-1} IL-6, 20 ng ml^{-1} IL-23, 20 ng ml^{-1} IL-1β, 10 µg ml^{-1} anti-IL-4, 10 µg ml^{-1} anti-IFN-γ and 400 nM FICZ). Pifithrin-α, p-nitro and nutlin-3a were purchased from Santa Cruz Biotechnology and Tocris Biosciences, respectively.

IL-22 neutralization and reconstitution. Monoclonal anti-IL-22 (clone IL22JOP) blocking antibody and isotype control IgG2aκ (clone eBR2a) were purchased from Thermo Fisher Scientific. Mice were administered anti-IL-22 (50 µg per mouse) or isotype intraperitoneally every 48 h until the conclusion of the experiment. For recombinant IL-22 treatment, mice were injected with recombinant IL-22 (500 ng per mouse; PeproTech) intraperitoneally every 24 h until the conclusion of the experiment. Mice were administered these reagents at least five times before inducing PhZ-mediated anemia.

Cytokine quantitation. IL-22 in human samples was quantified using either Human IL-22 Quantikine ELISA kit (D2200, R&D Systems) or Single Molecule Counting (SMC) Human IL-22 High Sensitivity Immunoassay kit (EMD Millipore, 03-0162-00) according to manufacturers' instructions. The SMC assay was read on a SMC Pro (EMD Millipore) instrument. The lower limit of quantification of this immunoassay is 0.1 pg ml^{-1}. IL-22 in mouse samples was quantified using ELISA MAXTM Deluxe Set Mouse IL-22 (BioLegend, 436304). The lower limit of quantification of this immunoassay is 3.9 pg ml^{-1}. S100A8 in human samples was quantified using Human S100A8 DuoSet ELISA (DY4570, R&D Systems).

Concentration of lineage-associated cytokines in cell culture supernatants of polarized T cells were quantified using a custom-made ProCarta Plex assay (Thermo Fisher Scientific) acquired on a Luminex platform. Hepcidin in mouse serum was quantified using a colorimetric assay from Hepcidin Murine-Compete ELISA kit from Intrinsic LifeSciences (HMC-001).

mRNA quantitation. Cells were flow sorted directly into the lysis buffer provided with the Cells-to-CT 1-Step TaqMan kit (Thermo Fisher Scientific, A25605) and processed according to the manufacturer's instructions. Pre-designed TaqMan

gene expression assays were used to quantify mRNA expression by qPCR using QuantStudio 6 (Thermo Fisher Scientific). *Hprt* was used as housekeeping control. Relative expression was calculated using the ΔCt method. Supplementary Table 4 describes primer details.

Chromatin immunoprecipitation. ChIP was performed using EZ-ChIP kit (EMD Millipore) according to manufacturer's instructions. Briefly, cells were fixed and cross-linked with 1% formaldehyde at 25 °C for 10 min and quenched with 125 mM glycine for an additional 10 min. Cell pellets were resuspended in lysis buffer and shearing was carried out using the Diagenode Bioruptor sonication system for a total of 40 cycles. Pre-cleared lysates were incubated with control Mouse IgG or anti-p53 (Santa Cruz Biotechnology) antibodies. The *Il22* promoter-specific primer pair was designed using Primer 3.0 Input as follows:

Forward primer: 5′ CCAAACTTAACTTGACCTTGGC 3′
Reverse primer: 5′ TTCTTCACAGCTCCCA TTGC 3′

In vitro erythroid differentiation. Whole BM cells were labeled with biotin-conjugated lineage antibodies (cocktail of anti-CD3ε, anti-CD11b, anti-CD45R/B220, anti-Gr1, anti-CD5 and anti-TER-119) (BD Pharmingen) and purified using anti-biotin beads and negative selection on the AutoMACS Pro (Miltenyi). Purified cells were then seeded in fibronectin-coated (2 μg cm^{-2}) tissue-culture-treated polystyrene wells (Corning BioCoat Cellware) at a cell density of 10^5 ml^{-1}. Erythroid differentiation was carried out according to modified published protocols[56]. The erythropoietic medium was IMDM supplemented with erythropoietin at 10 U ml^{-1}, 10 ng ml^{-1} stem cell factor (PeproTech), 10 μM dexamethasone (Sigma-Aldrich), 15% FBS, 1% detoxified BSA (StemCell Technologies), 200 μg ml^{-1} holotransferrin (Sigma-Aldrich), 10 mg ml^{-1} human insulin (Sigma-Aldrich), 2 mM L-glutamine, 0.1 mM β-mercaptoethanol and penicillin-streptomycin. After 48 h, the medium was replaced by IMDM containing 20% FBS, 2 mM L-glutamine, 0.1 mM β-mercaptoethanol and penicillin-streptomycin. Then, 50% of the culture medium was replaced after 48 h and cell density was maintained at 0.5×10^6 ml^{-1}. The total culture period for the assay was 6 d. Recombinant mouse IL-22 (PeproTech/Cell Signaling) was used where indicated. RII–RIV populations were gated as shown in Extended Data Fig. 2a.

Proteomic profiling. Proteomic profiling of sort-purified erythroid progenitors was performed as described elsewhere[30]. Briefly, cells were captured in collection microreactors and stored at −80 °C. Cell lysis was performed by adding 10 μl of 8 M urea, 10 mM TCEP and 10 mM iodoacetamide in 50 mM ammonium bicarbonate to the cell pellet of 1×10^6 erythroid progenitors and incubated at room temperature for 30 min, shaking in the dark. Then, 50 mM ammonium bicarbonate was used to dilute the urea to <2 M and the appropriate amount of trypsin for a 1:100 enzyme to substrate ratio was added and allowed to incubate at 37 °C overnight. Once digestion was completed, the lysate was spun through the glass mesh directly onto a C18 Stage tip (Empore[57]) at 3,500*g* until the entire digest passed through the C18 resin. Then, 75 μl 0.1% formic acid (FA) was used to ensure transfer of peptides to the C18 resin from the mesh while washing away lysis buffer components. C18-bound peptides were immediately subjected to on-column tandem mass tag (TMT) labeling.

On-column TMT labeling. Resin was conditioned with 50 μl methanol, followed by 50 μl 50% acetonitrile (ACN)/0.1% FA and equilibrated with 75 μl 0.1% FA twice. The digest was loaded by spinning at 3,500*g* until the entire digest passed through. One microliter of TMT reagent in 100% ACN was added to 100 μl freshly made HEPES (pH 8) and passed over the C18 resin at 350*g* until the entire solution passed through. HEPES and residual TMT was washed away with two applications of 75 μl 0.1% FA and peptides were eluted with 50 μl 50% ACN/0.1% FA followed by a second elution with 50% ACN/20 mM ammonium formate (NH_4HCO_2), pH 10. Peptide concentrations were estimated using an absorbance reading at 280 nm and checking of label efficiency was performed on 1/20th of the elution. After using 1/20th of the elution to test for labeling efficiency, the samples were mixed before fractionation and analysis.

Stage tip bSDB fractionation. First, 200-μl pipette tips were packed with two punches of sulfonated divinylbenzene (SDB-RPS; Empore) with a 16-gauge needle. After loading ~20 μg peptides in total, a pH switch was performed using 25 μl 20 mM NH_4HCO_2 (pH 10) and was considered part of fraction one. Then, step fractionation was performed using ACN concentrations of 5, 7.5, 10, 12.5, 15, 17.5, 20, 25, 42 and 50%. Each fraction was transferred to autosampler vials and dried via vacuum centrifugation and stored at 80 °C until analysis.

Data acquisition. Chromatography was performed using a Proxeon UHPLC at a flow rate of 200 nl min^{-1}. Peptides were separated at 50 °C using a 75-μm i.d. PicoFrit (New Objective) column packed with 1.9 μm AQ-C18 material (Dr. Maisch, Germany) to 20 cm in length over a 110-min run. The on-line LC gradient went from 6% B at 1 min to 30% B in 85 min, followed by an increase to 60% B by 94 min, then to 90% by 95 min and finally to 50% B until the end of the run. Mass spectrometry (MS) was performed on a Thermo Scientific Lumos Tribrid mass spectrometer. After a precursor scan from 350 to 1,800 *m*/*z* at 60,000 resolution, the topmost intense multiply charged precursors in a 2-s window were selected for higher energy collisional dissociation at a resolution of 50,000. Precursor isolation width was set to 0.7 *m*/*z* and the maximum MS2 injection time was 110 ms for an automatic gain control of 6×10^4. Dynamic exclusion was set to 45 s and only charge states two to six were selected for MS2. Half of each fraction was injected for each data acquisition run.

Data processing. Data were searched all together with Spectrum Mill (Agilent) using the Uniprot Mouse database (28 December 2017), containing common laboratory contaminants and 553 smORFs. A fixed modification of carbamidomethylation of cysteine and variable modifications of *N*-terminal protein acetylation, oxidation of methionine and TMT-11plex labels were searched. The enzyme specificity was set to trypsin and a maximum of three missed cleavages was used for searching. The maximum precursor-ion charge state was set to six. The MS1 and MS2 mass tolerance were set to 20 ppm. Peptide and protein FDRs were calculated to be <1% using a reverse, decoy database. Proteins were only reported if they were identified with at least two distinct peptides and a Spectrum Mill score protein level score ~ 20.

TMT11 reporter ion intensities in each MS/MS spectrum were corrected for isotopic impurities by the Spectrum Mill protein/peptide summary module using the afRICA correction method which implements determinant calculations according to Cramer's rule and general correction factors obtained from the reagent manufacturer's certificate of analysis.

Differential protein abundance analysis. The median normalized, median absolute deviation-scale dataset was subjected to a moderated F-test, followed by Benjamini–Hochberg procedure correcting for multiple hypothesis testing. We drew an arbitrary cutoff at adjusted $P<0.05$.

RNA-sequencing. A total of 5,000 IL-22 $^+$(CD4$^+$IL-22(tdtomato)$^+$) cells were FACS sorted directly into TLC Buffer (QIAGEN) with 1% β-mercaptoethanol. For the preparation of libraries, cell lysates were thawed and RNA was purified with 2.2× RNAClean SPRI beads (Beckman Coulter Genomics) without final elution[58]. The RNA captured beads were air-dried and processed immediately for RNA secondary structure denaturation (72 °C for 3 min) and complementary DNA synthesis. SMART-seq2 was performed on the resultant samples following the published protocol[59] with minor modifications in the reverse transcription step. A 15-μl reaction mix was used for subsequent PCR and performed ten cycles for cDNA amplification. The amplified cDNA from this reaction was purified with 0.8× Ampure SPRI beads (Beckman Coulter Genomics) and eluted in 21 μl TE buffer. We used 0.2 ng cDNA and one-eighth of the standard Illumina NexteraXT (Illumina FC-131-1096) reaction volume to perform both the tagmentation and PCR indexing steps. Uniquely indexed libraries were pooled and sequenced with NextSeq 500 high output V2 75 cycle kits (Illumina FC-404-2005) and 38×38 paired-end reads on the NextSeq 500 instrument. Reads were aligned to the mouse mm10 transcriptome using Bowtie[60] and expression abundance transcripts per million estimates were obtained using RSEM[61].

Pathway analysis. GSEA was performed with Broad Institute's GSEA Software[62]. The 'IL-22_Signature' and 'Rps14_Increased' gene sets were created from the literature[10,63] (Fig. 2c,f). Full lists of genes in the individual gene sets can be found in Supplementary Table 1. Other reference gene sets are available from MSigDB[64]. For GSEA analyses, mouse UniProt IDs were converted to their orthologous human gene symbols using MSigDB 7.1 ChIP file mappings. Pathway enrichment (Fig. 2e) was performed using Clarivate Analytics' MetaCore software[65].

Microarray data analysis. Microarray data of CD34$^+$ cells from healthy controls and patients with del(5q) and non-del(5q) MDSs were obtained from a previously published study[66] submitted in Gene Expression Omnibus[67,68] accessible under GSE19429.

Statistical tests. Data are presented as mean ± s.e.m. unless otherwise indicated. Comparison of two groups was performed using paired or unpaired two-tailed Student's *t*-test. For multiple group comparisons, ANOVA with Tukey's correction or Kruskal–Wallis test with Dunn's correction was depending on data requirements. Statistical analyses were performed using GraphPad Prism v.8.0 (GraphPad Software). A *P* value <0.05 was considered significant.

Reporting Summary. Further information on research design is available in the Nature Research Reporting Summary linked to this article.

Data availability

The original mass spectra may be downloaded from MassIVE (http://massive.ucsd.edu), MSV000085287. The data are directly accessible via ftp://massive.ucsd.edu/MSV000085287/. Raw RNA-seq data are accessible via Gene Expression Omnibus under accession code GSE165467. Source data for all applicable figures (main and extended) are provided with the paper. The remaining data supporting the findings of this study are available from the corresponding authors upon reasonable request. Materials will be provided with material transfer agreements as appropriate. Source data are provided with this paper.

References

51. Skarnes, W. C. et al. A conditional knockout resource for the genome-wide study of mouse gene function. *Nature* **474**, 337–342 (2011).
52. Farley, F. W., Soriano, P., Steffen, L. S. & Dymecki, S. M. Widespread recombinase expression using FLPeR (flipper) mice. *Genesis* **28**, 106–110 (2000).
53. Heinrich, A. C., Pelanda, R. & Klingmüller, U. A mouse model for visualization and conditional mutations in the erythroid lineage. *Blood* **104**, 659–666 (2004).
54. Savage, A. K., Liang, H. E. & Locksley, R. M. The development of steady-state activation hubs between adult LTi ILC3s and primed macrophages in small intestine. *J. Immunol.* **199**, 1912–1922 (2017).
55. Pronk, C. J. et al. Elucidation of the phenotypic, functional, and molecular topography of a myeloerythroid progenitor cell hierarchy. *Cell Stem Cell* **1**, 428–442 (2007).
56. Shuga, J., Zhang, J., Samson, L. D., Lodish, H. F. & Griffith, L. G. In vitro erythropoiesis from bone marrow-derived progenitors provides a physiological assay for toxic and mutagenic compounds. *Proc. Natl Acad. Sci. USA* **104**, 8737–8742 (2007).
57. Rappsilber, J., Ishihama, Y. & Mann, M. Stop and go extraction tips for matrix-assisted laser desorption/ionization, nanoelectrospray, and LC/MS sample pretreatment in proteomics. *Anal. Chem.* **75**, 663–670 (2003).
58. Shalek, A. K. et al. Single-cell transcriptomics reveals bimodality in expression and splicing in immune cells. *Nature* **498**, 236–240 (2013).
59. Picelli, S. et al. Smart-seq2 for sensitive full-length transcriptome profiling in single cells. *Nat. Methods* **10**, 1096–1098 (2013).
60. Langmead, B., Trapnell, C., Pop, M. & Salzberg, S. L. Ultrafast and memory-efficient alignment of short DNA sequences to the human genome. *Genome Biol.* **10**, R25 (2009).
61. Li, B. & Dewey, C. N. RSEM: accurate transcript quantification from RNA-seq data with or without a reference genome. *BMC Bioinf.* **12**, 323 (2011).
62. Subramanian, A. et al. Gene set enrichment analysis: a knowledge-based approach for interpreting genome-wide expression profiles. *Proc. Natl Acad. Sci. USA* **102**, 15545–15550 (2005).
63. Dudakov, J. A., Hanash, A. M. & van den Brink, M. R. Interleukin-22: immunobiology and pathology. *Annu. Rev. Immunol.* **33**, 747–785 (2015).
64. Liberzon, A. et al. Molecular signatures database (MSigDB) 3.0. *Bioinformatics* **27**, 1739–1740 (2011).
65. Nikolsky, Y., Ekins, S., Nikolskaya, T. & Bugrim, A. A novel method for generation of signature networks as biomarkers from complex high throughput data. *Toxicol. Lett.* **158**, 20–29 (2005).
66. Pellagatti, A. et al. Deregulated gene expression pathways in myelodysplastic syndrome hematopoietic stem cells. *Leukemia* **24**, 756–764 (2010).
67. Barrett, T. et al. NCBI GEO: archive for functional genomics data sets–update. *Nucleic Acids Res.* **41**, D991–D995 (2013).
68. Edgar, R., Domrachev, M. & Lash, A. E. Gene expression omnibus: NCBI gene expression and hybridization array data repository. *Nucleic Acids Res.* **30**, 207–210 (2002).

Acknowledgements

We thank R. Caspi (National Eye Institute, US NIH) and Genentech for providing *Il22* knockout mice; B. L. Ebert (DFCI) for providing Rps14-floxed mice; R. Locksley (University of California San Francisco) for providing *Catch-22* mice; and U. Klingmüller (Deutsches Krebsforschungszentrum) for providing *Epor*-cre mice. We also thank the Animal Resources Facility, the Ted and Eileen Pasquarello Tissue Bank in Hematologic Malignancies and flow cytometry core facility at DFCI for their valuable technical assistance. We thank E. Smith for assistance with creating the graphical illustration. We thank P. Májek (Ústav hematologie a krevní transfuse) for providing plasma proteomic profiling data of healthy controls and patients with MDSs. This work was supported by a Discovery Research Grant from the Edward P. Evans Foundation (to L.H.G.) and institutional funding from DFCI (to L.H.G). D.P.S. is supported by the Edward P. Evans Foundation and by NIH Leukemia SPORE 1P50CA206963 and 2P01CA066996. This work was supported in part by grants from the National Cancer Institute (NCI) Clinical Proteomic Tumor Analysis Consortium grants NIH/NCI U24-CA210986 and NIH/NCI U01 CA214125 (to S.A.C.).

Author contributions

M.R. and L.H.G. conceived the study, designed experiments, analyzed the data and wrote the manuscript; M.R. performed the experiments; S.G. assisted with in vitro experiments; S.A.M. performed proteomic profiling and data analysis; M.S.C. performed RNA-seq; M.S. processed RNA-seq data; S.A.C. analyzed proteomic profiling data; S.S.W. and J.V.B. collected CKD patient samples and related clinical information and analyzed the data; J.R., R.M.S. and D.P.S. collected MDS patient samples and related clinical information and analyzed the data; and A.R. supervised RNA-seq experiments and analyzed data.

Competing interests

An invention disclosure has been filed based on the data generated in this study. From 4 August 2020, Meromit Singer has been an employee of Guardant Health. S.S.W. has served on the steering committee of a GSK trial on an oral hypoxia-inducible factor prolyl hydroxylase inhibitor, as a potential treatment for anemia associated with CKD; S.S.W. has also received consulting fees from Public Health Advocacy Institute, CVS, Roth Capital Partners, Kantum Pharma, Mallinckrodt, Wolters Kluewer, GE Health Care, Allena Pharmaceuticals, Mass Medical International, JNJ, Venbio, Strataka, Takeda, Cerus and Pfizer. D.P.S. has served on independent data safety monitoring committees for clinical trials supported by Takeda, Astex, Janssen and Onconova; has consulted for Celgene and Daiichi Sankyo; and has received research support (to the institution) for clinical trials sponsored by Aprea, H3 Biosciences, Syros and Astra Zeneca. J.R. reports research funding from Amgen, Equillium and Kite Pharma; and consulting income from Aleta Biotherapeutics, Avrobio, Celgene, Falcon Therapeutics, LifeVault Bio, Rheos Medicines, Talaris Therapeutics and TScan Therapeutics. R.M.S. has served on independent data safety monitoring committees for trials supported by Celgene, Takeda and Argenix; has consulted for AbbVie, Actinium, Agios, Amgen, Arog, Astellas, Astra Zeneca, Biolinerx, Celgene, Daiichi Sankyo, Fujifilm, Janssen, Juno, Macrogenics, Novartis, Ono, Orsenix, Pfizer, Roche, Stemline, Sumitomo, Takeda and Trovagene; and has received research support (to the institution) for clinical trials sponsored by AbbVie, Agios, Arog and Novartis. S.A.C. is a member of the scientific advisory boards of Kymera, PTM BioLabs and Seer and is a scientific advisor to Pfizer and Biogen. A.R. is a Scientific Advisory Board member of Thermo Fisher Scientific, Neogene Therapeutics, Asimov and Syros Pharmaceuticals. A.R. is a cofounder of and equity holder in Celsius Therapeutics and an equity holder in Immunitas. From 1 August 2020, A.R. has been an employee of Genentech. L.H.G. is a former Director of Bristol-Myers Squibb and the Waters Corporation and is currently on the board of directors of and holds equity in GlaxoSmithKline Pharmaceuticals and Analog Devices. She also serves on the scientific advisory boards of Repare Therapeutics, Abpro Therapeutics and Kaleido Therapeutics. S.A.C. is a member of the scientific advisory boards of Kymera, PTM BioLabs, and Seer and is a scientific advisor to Pfizer and Biogen. All other authors declare no competing interests.

Additional information

Extended data is available for this paper at https://doi.org/10.1038/s41590-021-00895-4.

Supplementary information The online version contains supplementary material available at https://doi.org/10.1038/s41590-021-00895-4.

Correspondence and requests for materials should be addressed to M.R. or L.H.G.

Peer review information *Nature Immunology* thanks Michaëla Fontenay, Rebekka Schneider and the other, anonymous reviewer(s) for their contribution to the peer review of this work. L. A. Dempsey was the primary editor on this article and managed its editorial process and peer review in collaboration with the rest of the editorial team.

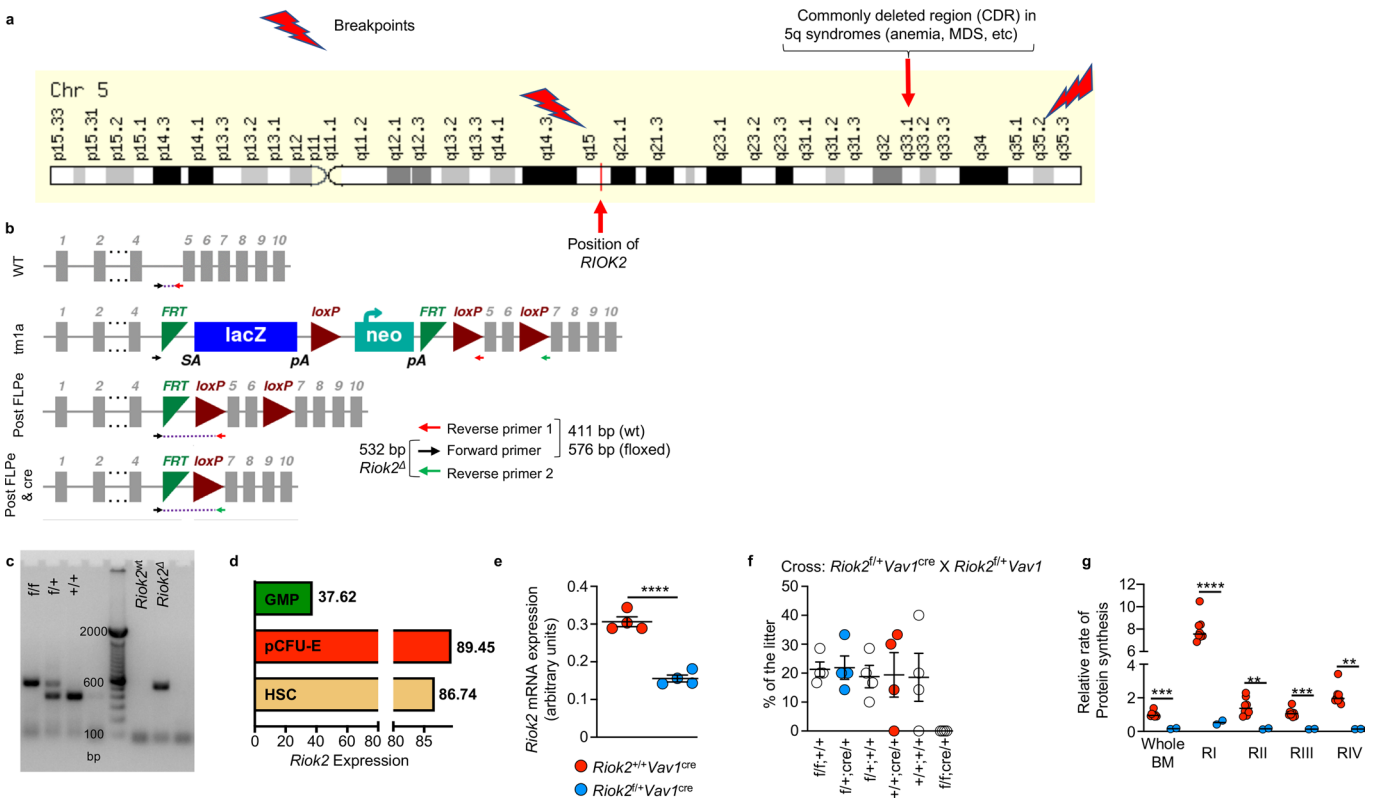

Extended Data Fig. 1 | Localization and expression of *Riok2*. **a**, Location of *RIOK2* gene on human chromosome 5. **b**, Schematic representation of the *Riok2*$^{tm1a(KOMP)Wtsi}$ allele and generation of *Riok2* floxed mice. **c**, Agarose gel showing genotyping of *Riok2* floxed mice. *Riok2*$^{\Delta}$ indicates deletion of *Riok2*. No band expected in the *Riok2*^{wt} lane. **d**, Expression of *Riok2* mRNA in mouse BM cells. Modified from Gene Expression Commons. Numbers next to bars indicate expression level. **e**, *Riok2* mRNA expression by qRT-PCR in BM cells from *Riok2* haploinsufficient mice and *Vav1*^{cre} controls. n = 5 mice/group. **f**, Frequency of the genotypes indicated on the X-axis among 4 litters from 4 different breeding crosses of the genotypes mentioned. **g**, *In vivo* protein synthesis rates in the indicated cell types from *Riok2* haploinsufficient mice (n = 2) and *Vav1*^{cre} controls (n = 8). Unpaired two-tailed *t*-test (e), multiple unpaired two-tailed *t*-tests with Holm-Sidak method (g) used to calculate statistical significance. Data are shown as mean ± s.e.m (e,f) or mean ± s.d. **g**, and are representative of two (e, g) or four (c, f) independent experiments. ** $p < 0.01$, *** $p < 0.001$, **** $p < 0.0001$.

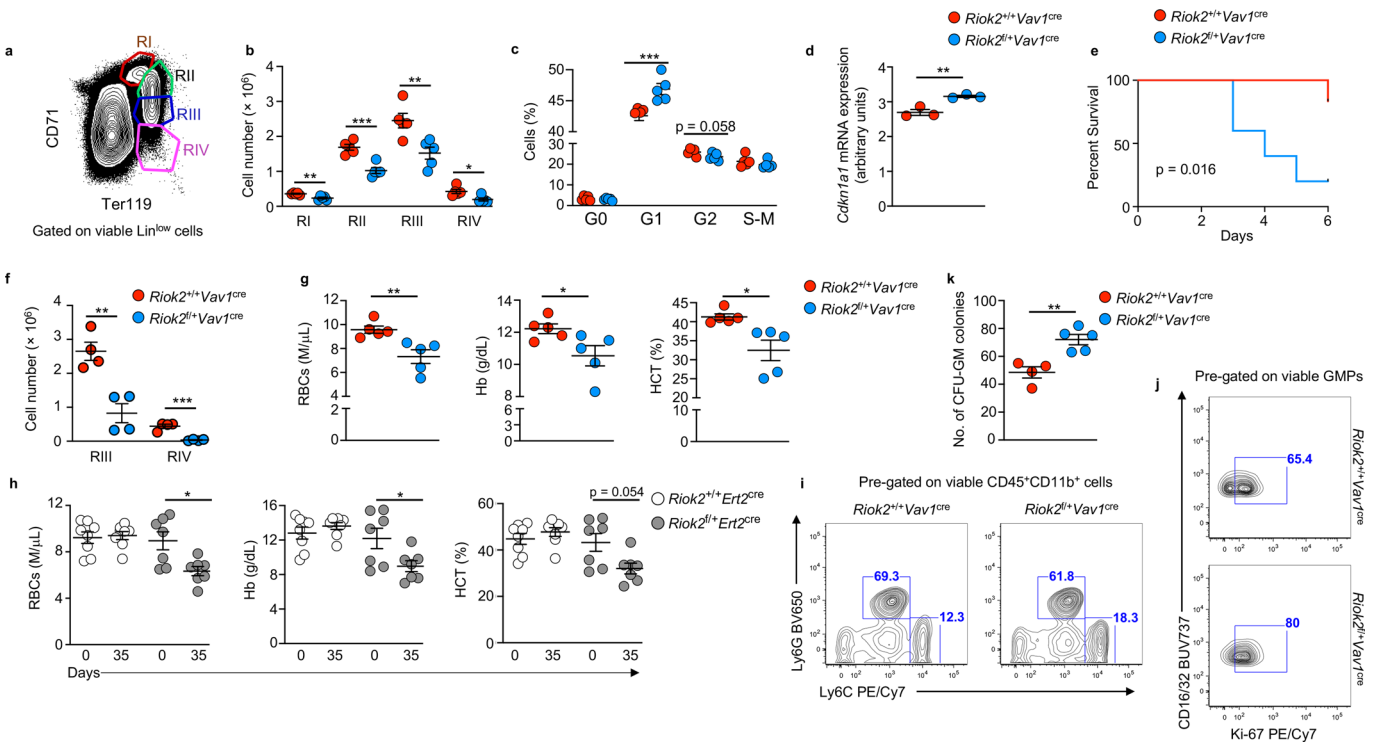

Extended Data Fig. 2 | *Riok2* haploinsufficient mice display anemia and myeloproliferation. a, Gating strategy used for the identification of erythroid progenitor/ precursor cells in the BM. **b**, Number of erythroid progenitor populations among viable BM cells in *Riok2*$^{fl/+}$*Vav1*^{cre} mice and *Riok2*$^{+/+}$*Vav1*^{cre} controls. n = 5/group. **c**, Cell cycle analysis of erythroid progenitor/ precursor cells from *Riok2* haploinsufficient mice in comparison to *Vav1*^{cre} controls. n = 5 mice/group. **d**, *Cdkn1a* mRNA expression by qRT-PCR in erythroid progenitors from *Riok2* haploinsufficient mice and *Vav1*^{cre} controls. n = 3 mice/ group. **e**, Kaplan-Meier survival curve for *Riok2* haploinsufficient mice and *Vav1*^{cre} controls subjected to lethal dose of PhZ. **f**, Number of RIII and RIV erythroid precursor populations among viable BM cells in *Riok2*$^{fl/+}$*Vav1*^{cre} mice and *Riok2*$^{+/+}$*Vav1*^{cre} controls day 6 after PhZ treatment. n = 4/group. **g**, PB RBC numbers, Hb, and HCT in mice transplanted with either *Riok2* haploinsufficient mice or *Vav1*^{cre} BM cells. n = 5 mice/group. **h**, PB RBC numbers, Hb, and HCT in mice with tamoxifen-inducible deletion of *Riok2*. Tamoxifen administered on days 3 – 7. n = 8 and 7 for *Riok2*$^{+/+}$*Ert2*^{cre} and *Riok2*$^{fl/+}$*Ert2*^{cre} mice, respectively. **i**, Representative flow cytometry plots showing frequency of monocytes (CD11b^{+}Ly6G^{-}Ly6C^{hi}) and neutrophils (CD11b^{+}Ly6G^{+}) in the PB of *Riok2*$^{fl/+}$*Vav1*^{cre} and *Riok2*$^{+/+}$*Vav1*^{cre} mice. **j**, Representative flow cytometry plots showing Ki-67^{+} GMPs in the BM of *Riok2*$^{fl/+}$*Vav1*^{cre} and *Riok2*$^{+/+}$*Vav1*^{cre} mice. **k**, Number of CFU-GM colonies in MethoCult from Lin^{-}Sca-1^{+}c-kit^{+} BM cells from *Riok2*$^{fl/+}$*Vav1*^{cre} mice (n = 5) and *Riok2*$^{+/+}$*Vav1*^{cre} controls (n = 4) after a 7-day culture period. n = 4-5/group. Multiple unpaired two-tailed *t*-tests with Holm-Sidak method (b, c), unpaired two-tailed *t*-test (d, f, g, k), log-rank test (e), and 2-way ANOVA with Sidak's correction for multiple comparisons (h) used to calculate statistical significance. Data are shown as mean ± s.e.m and are representative of two (b to k) independent experiments. * p<0.05, ** p<0.01, *** p<0.001.

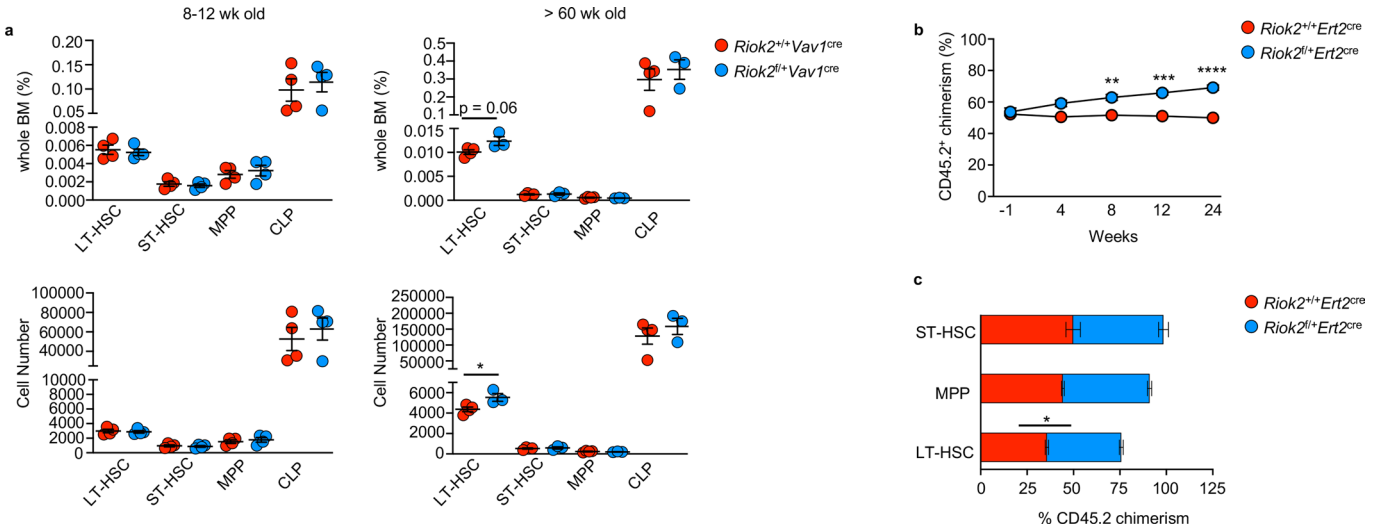

Extended Data Fig. 3 | *Riok2* haploinsufficiency alters early hematopoietic progenitors in an age-dependent fashion. a, Frequency and number of indicated cell types in the bone marrow of *Riok2*$^{fl/+}$*Vav1*^{cre} and *Riok2*$^{+/+}$*Vav1*^{cre} mice. n = 4/group. LT-HSC=long term hematopoietic stem cells, ST-HSC=short term hematopoietic stem cells, MPP=multipotent progenitors, CLP=common lymphoid progenitors. **b**, % CD45.2 (donor) chimerism in PB from competitive BM transplant with CD45.1 recipient cells. Time point '-1' reflects first bleeding 4 weeks after transplantation and one day before tamoxifen induced deletion of *Riok2*. Donor (CD45.2) chimerism of the HSC compartment in the BM of competitive transplantation experiments. n = 5/group. **c**, Frequency of donor (CD45.2$^+$) early hematopoietic progenitors 24 weeks after tamoxifen treatment in a competitive transplantation assay as described in (b). n = 5 and 4 for *Riok2*$^{+/+}$*Ert2*^{cre} and *Riok2*$^{fl/+}$*Ert2*^{cre} mice, respectively. Unpaired two-tailed *t*-test (a, c) and 2-way ANOVA with Sidak's multiple comparison test (b) used to calculate statistical significance. Data are shown as mean ± s.e.m and are representative of two (a-c) independent experiments. * p<0.05, ** p<0.01, *** p<0.001, **** p<0.0001.

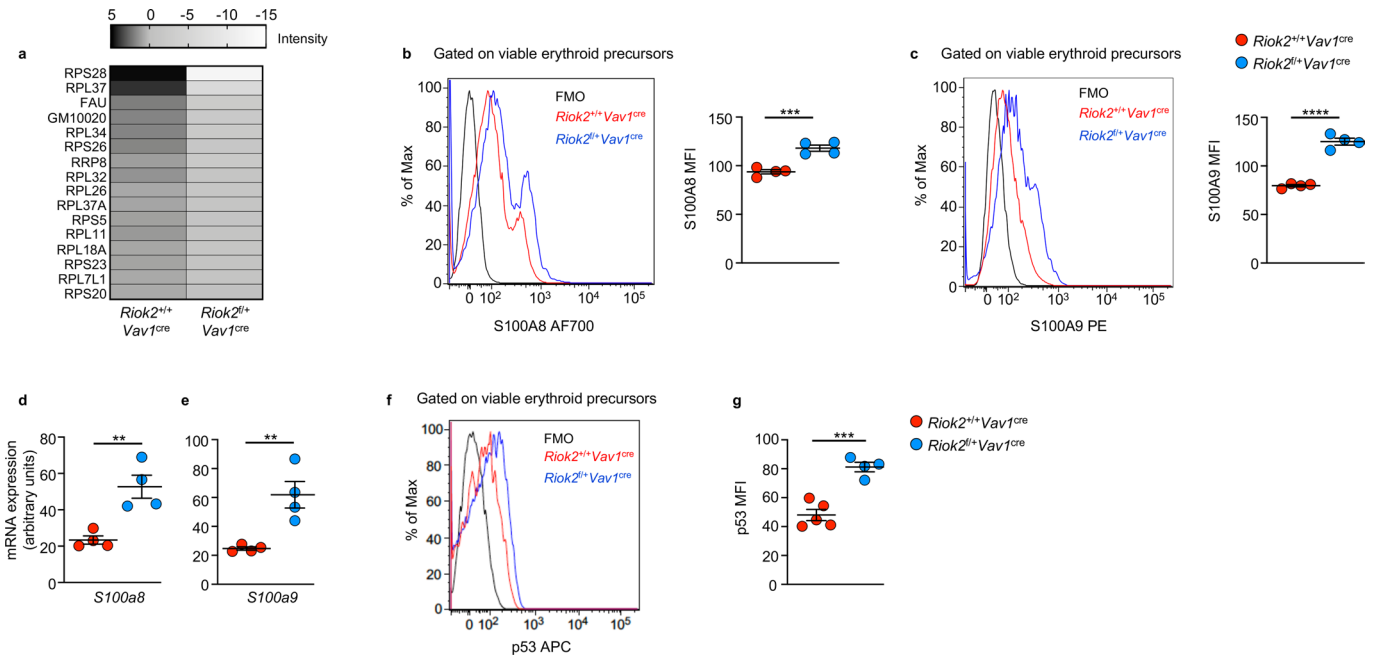

Extended Data Fig. 4 | *Riok2* haploinsufficient erythroid precursors express increased S100 proteins. (**a**) Expression of ribosomal proteins quantified by proteomics in *Riok2*$^{fl/+}$*Vav1*^{cre} and *Riok2*$^{+/+}$*Vav1*^{cre} erythroid precursors. S100A8 (**b**) and S100A9 (**c**) expression assessed by flow cytometry in BM erythroid precursors from *Riok2*$^{fl/+}$*Vav1*^{cre} and *Riok2*$^{+/+}$*Vav1*^{cre} mice. n = 4mice/group. **d**,**e**, *S100a8* and *S100a9* mRNA expression in erythroid precursors isolated from *Riok2*$^{fl/+}$*Vav1*^{cre} and *Riok2*$^{+/+}$*Vav1*^{cre} mice. n = 4 mice/group. **f**, p53 expression assessed by flow cytometry in BM erythroid precursors from *Riok2*$^{fl/+}$*Vav1*^{cre} and *Riok2*$^{+/+}$*Vav1*^{cre} mice. **g**, Graphical representation of data shown in (e). n = 5 mice/group. Data are shown as mean ± s.e.m and are representative of two (b to g) independent experiments. Unpaired two-tailed *t*-test (b to g) used to calculate statistical significance. ** p<0.01, *** p<0.001, **** p<0.0001.

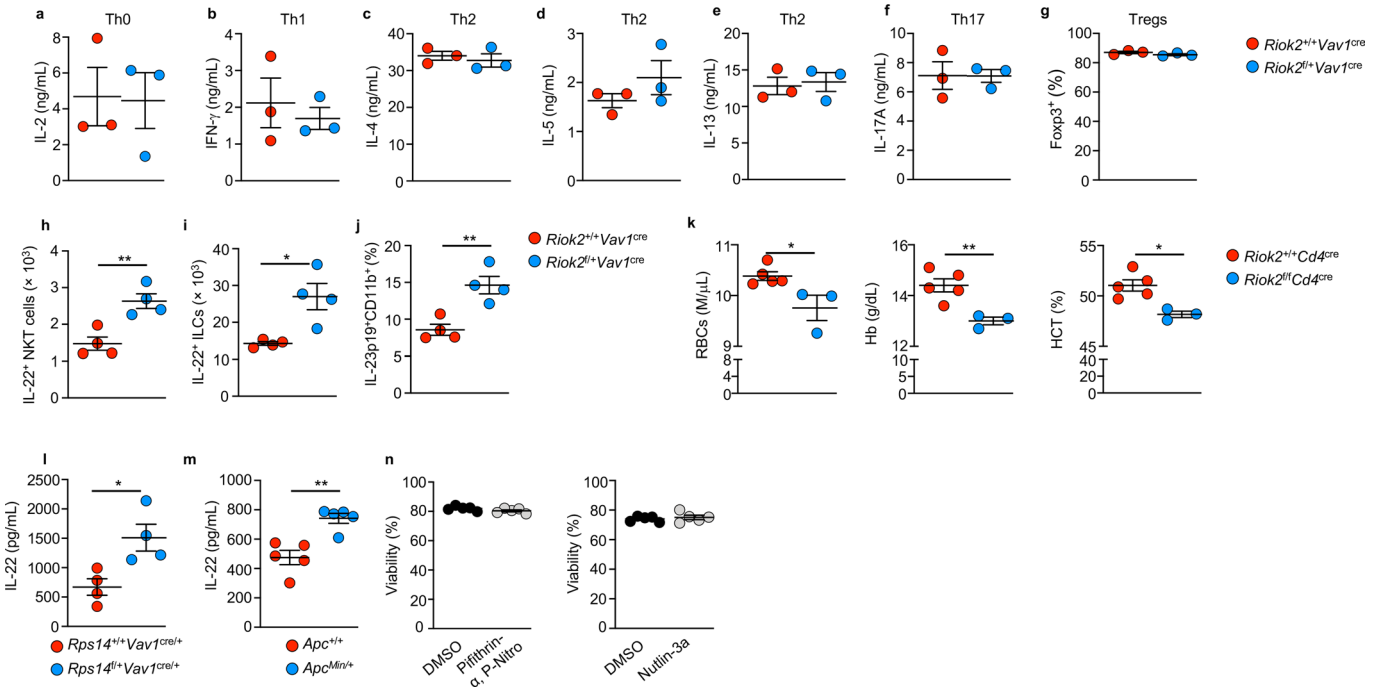

Extended Data Fig. 5 | Expression of lineage-associated T cell cytokines is comparable between *Riok2* haploinsufficient and sufficient T cells. a-g, Concentration of IL-2 (**a**), IFN-γ (**b**), IL-4 (**c**), IL-5 (**d**), IL-13 (**e**), IL-17A (**f**) and frequency of Foxp3$^+$ cells (**g**) from *in vitro* polarized T cells of the indicated genotypes. n = 3 mice/group. **h-i**) Number of IL-22$^+$ NKT cells (H) and ILCs (I) in the spleens of *Riok2*$^{f/+}$*Vav1*^{cre} mice and *Riok2*$^{+/+}$*Vav1*^{cre} controls (n = 4/group). **j**, Frequency of IL_23p19$^+$ DCs in *Riok2*$^{f/+}$*Vav1*^{cre} mice and *Riok2*$^{+/+}$*Vav1*^{cre} controls. n = 4 mice/group. **k**, PB RBC numbers, Hb, and HCT in *Riok2*$^{f/f}$*Cd4*^{cre} mice (n = 3) in comparison to *Riok2*$^{+/+}$*Cd4*^{cre} controls (n = 5). **l**, Secreted IL-22 from *in vitro* polarized T_H22 cells from *Rps14* haploinsufficient mice and *Vav1*^{cre} controls. n = 4 mice/group. **m**, Secreted IL-22 from *in vitro* polarized T_H22 cells from *Apc*^{Min} mice and littermate controls. n = 4 mice/group. **n**, Viable cells (expressed as percentage of total cells in culture) for the indicated treatments assessed by flow cytometry. n = 5 mice/group. Data are shown as mean ± s.e.m and are representative of two (a to n) independent experiments. Unpaired two-tailed *t*-test (a to n) used to calculate statistical significance. * $p < 0.05$, ** $p < 0.01$.

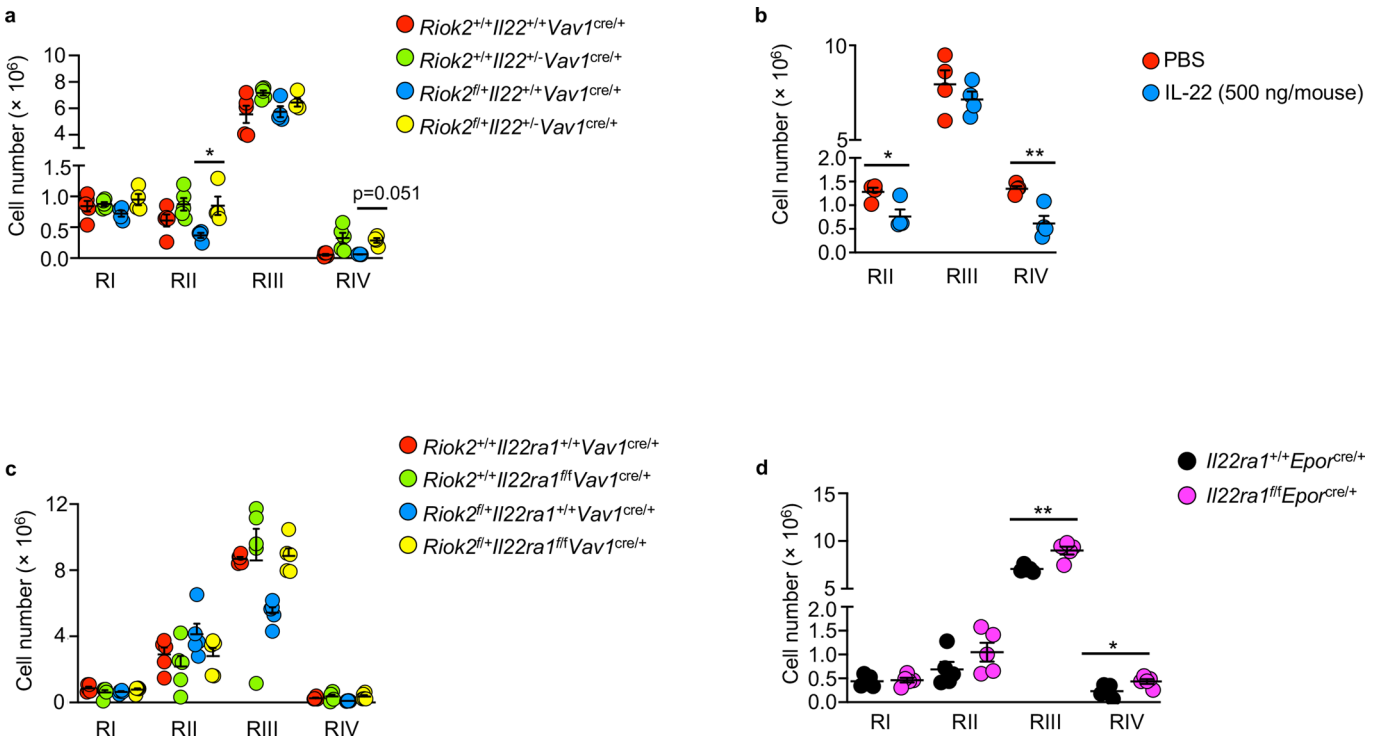

Extended Data Fig. 6 | Neutralization of IL-22 signaling increases number of erythroid precursors. a-d, Number of RI-RIV erythroid populations among viable BM cells in the indicated strains undergoing PhZ-induced stress erythropoiesis. For (a), n = 5,5,4, and 4 for *Riok2*$^{+/+}$*Il22*$^{+/+}$*Vav1*^{cre}, *Riok2*$^{+/+}$*Il22*$^{+/-}$*Vav1*^{cre}, *Riok2*$^{fl/+}$*Il22*$^{+/+}$*Vav1*^{cre}, *Riok2*$^{fl/+}$*Il22*$^{+/-}$*Vav1*^{cre}, respectively. For (d), n = 5/group. Data are shown as mean ± s.e.m and are representative of three (a, c) or two (b, d) independent experiments. 1-way ANOVA with Tukey's correction (a, c) or unpaired two-tailed *t*-test (b, d) used to calculate statistical significance. * $p < 0.05$, ** $p < 0.01$.

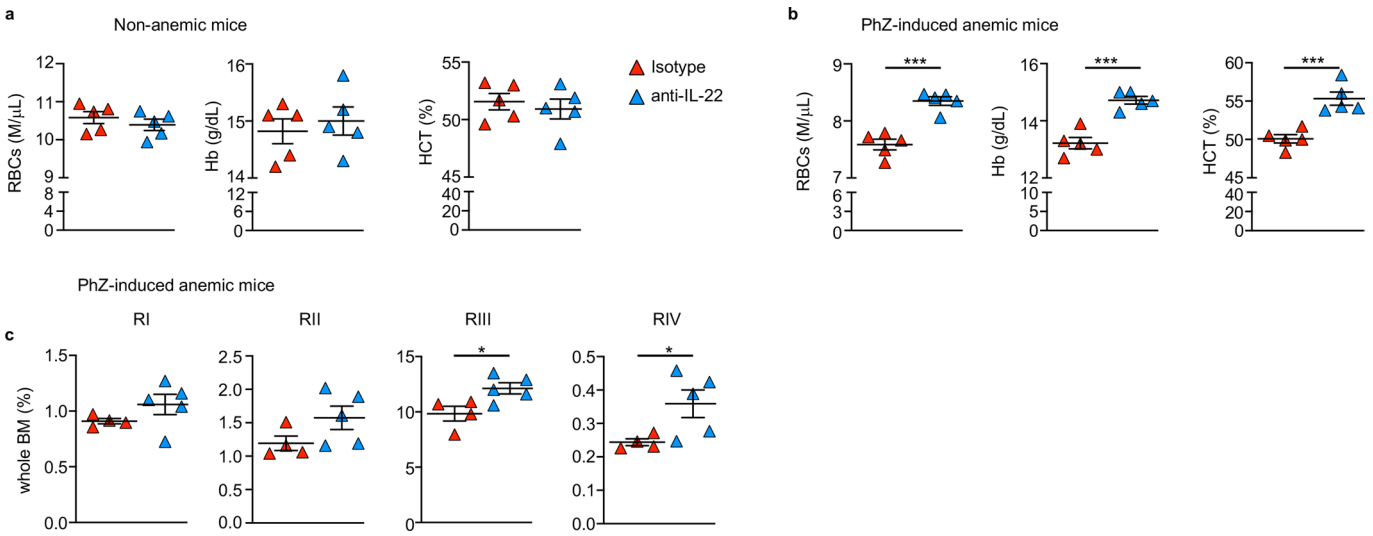

Extended Data Fig. 7 | IL-22 neutralization alleviates anemia in wt mice undergoing PhZ-induced stress erythropoiesis. a, PB RBC numbers, Hb, and HCT in naïve wt C57BL/6 J mice treated with isotype control (Rat IgG2aκ, 50 mg/mouse) or anti-IL-22 antibody (50 mg/mouse). n = 5 mice/group. **b**, PB RBC numbers, Hb, and HCT in wt C57BL/6 J mice undergoing PhZ-induced stress erythropoiesis treated with isotype control or anti-IL-22 antibody. n = 5 mice/group. **c**, Percentage of RI-RIV erythroid precursors in the BM of mice treated as in (**b**). n = 4 and 5 for *Il22ra1*$^{+/+}$*Epor*^{cre} and *Il22ra1*$^{f/f}$*Epor*^{cre} mice, respectively. Data are shown as mean ± s.e.m and are representative of three (a, b) or two (c) independent experiments. Unpaired two-tailed *t*-test (a to c) used to calculate statistical significance. * $p<0.05$, *** $p<0.001$.

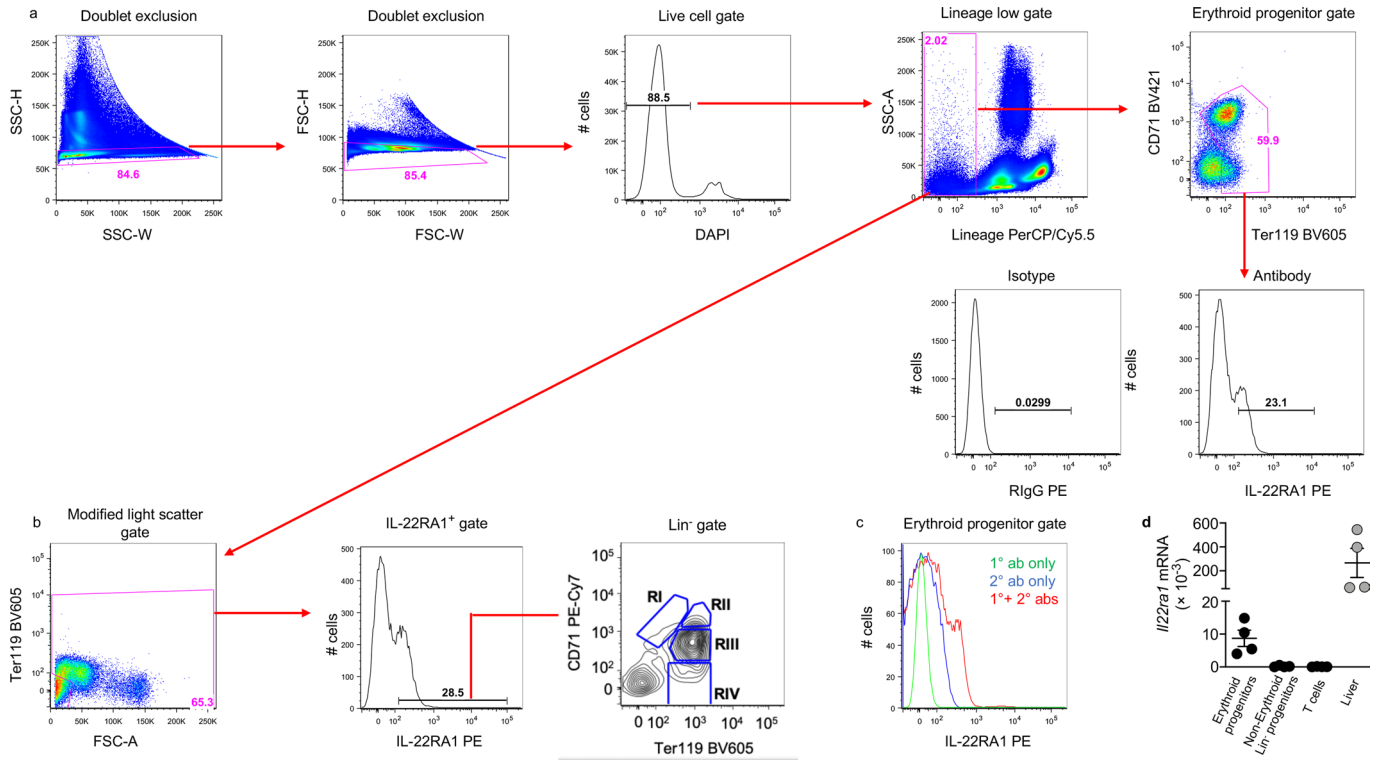

Extended Data Fig. 8 | Erythroid precursors express IL-22RA1. a, Gating strategy employed for assessing IL-22RA1 expression on erythroid precursors. **b**, Gating strategy to show that majority of IL-22RA1$^+$ cells in the mouse BM are erythroid precursors. **c**, IL-22RA1 expression on erythroid precursors assessed using flow cytometry and a second antibody targeting a different epitope of IL-22RA1. **d**, *Il22ra1* mRNA expression in the indicated cell types assessed by qRT-PCR. T cells and liver represent negative and positive controls, respectively. n = 4 mice/group. Data are shown as mean ± s.e.m (d) and are representative of three (a to c) or two (d) independent experiments.

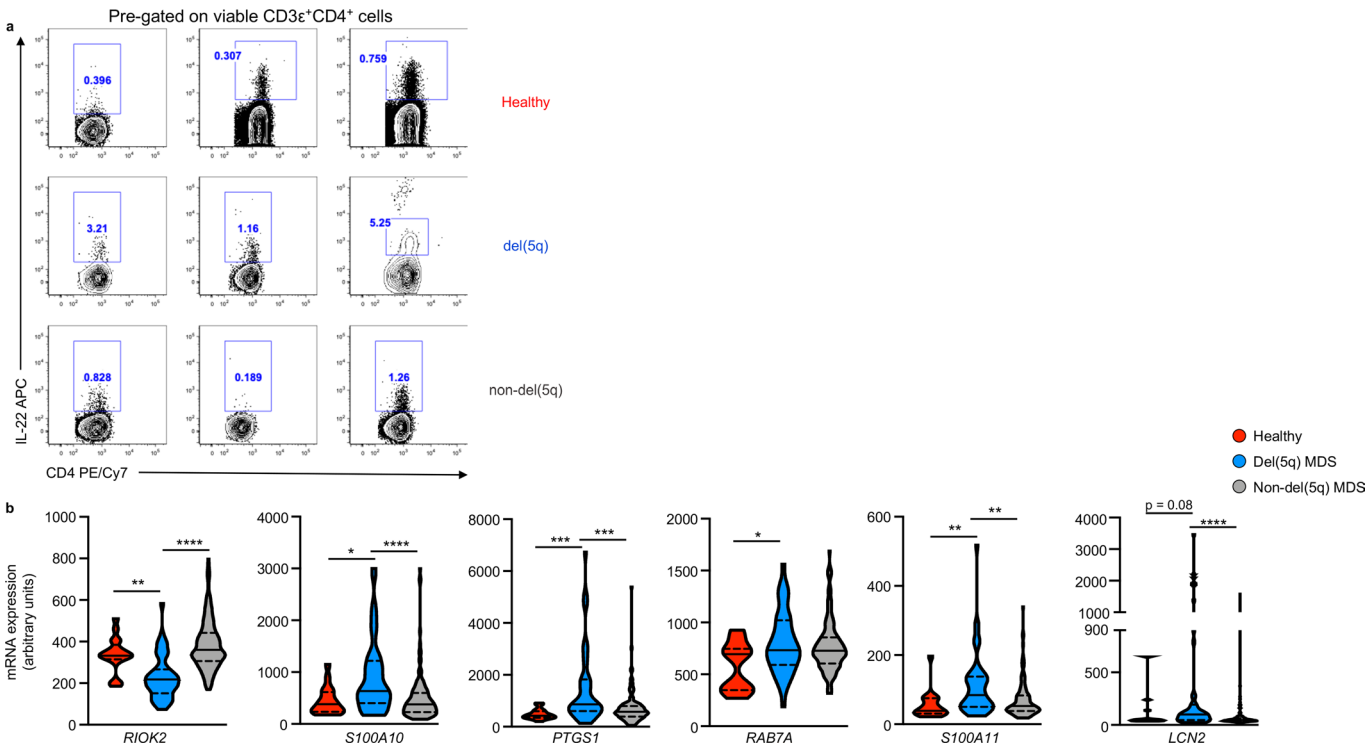

Extended Data Fig. 9 | Increased IL-22 and its signature genes in del(5q) MDS subjects. a, Representative flow cytometry plots showing frequency of CD4+IL-22+ cells among total PBMCs in the peripheral blood of MDS patients and healthy subjects. Pre-gated on viable CD3ε+CD4+ cells. Cumulative data shown in Fig. 4e. **b**, Expression of indicated IL-22 signature genes in CD34+ cells from healthy controls and del(5q) and non−del(5q) MDS patients. n = 17, 47, and 136 for healthy, del(5q) MDS, and non-del(5q) MDS, respectively. Kruskal-Wallis test with Dunn's correction for multiple comparisons (b) used to calculate statistical significance * p<0.05, ** p<0.01, *** p<0.001, **** p<0.0001. Solid lines represent median and dashed lines represent quartiles (b).

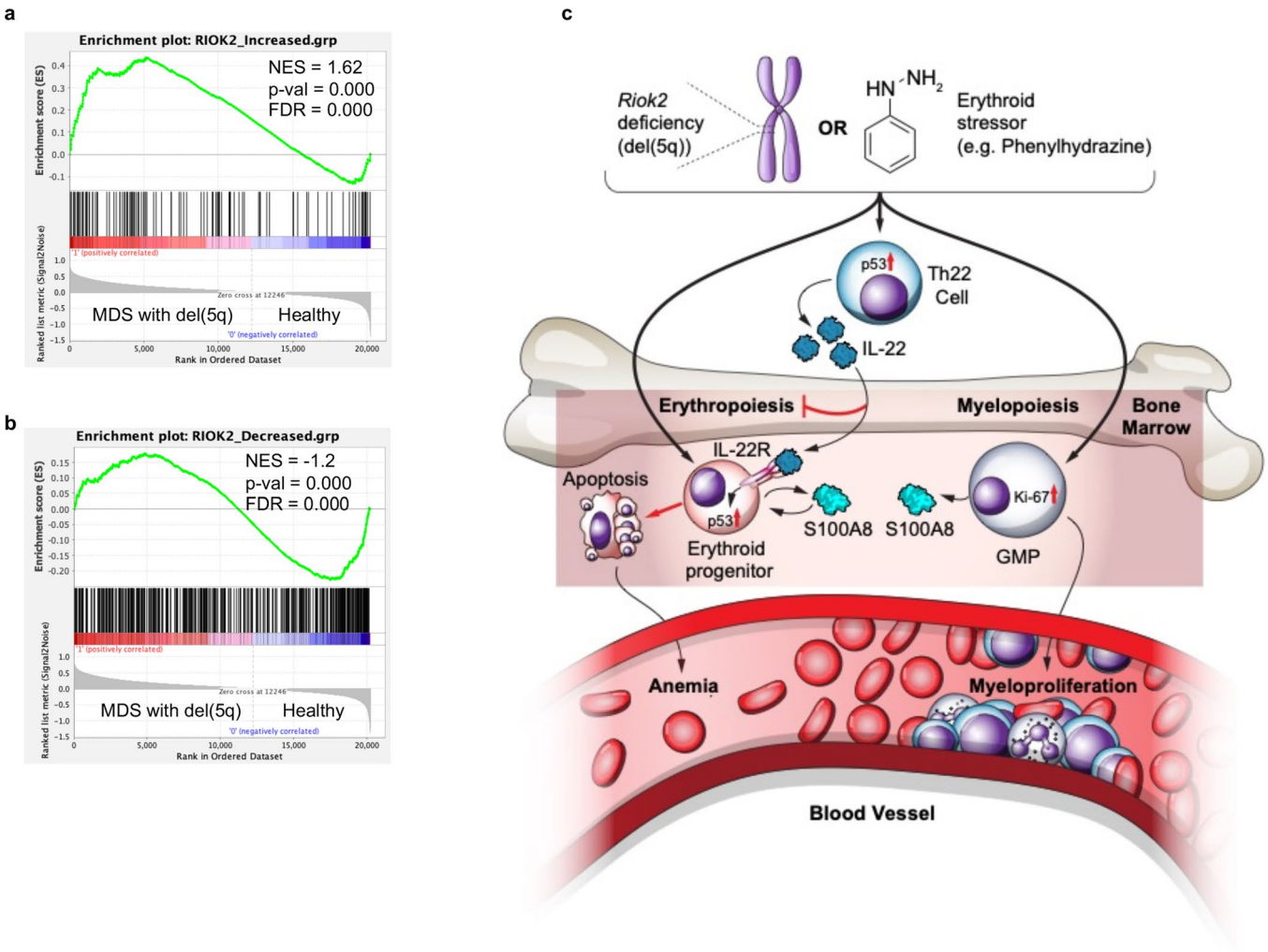

Extended Data Fig. 10 | *Riok2* haploinsufficiency recapitulates del(5q) MDS transcriptional changes. a,**b**, GSEA enrichment plots comparing proteins up-regulated (**a**) and down-regulated (**b**) upon *Riok2* haploinsufficiency to the transcriptional changes seen in del(5q) MDS. **c**, Schematic of mechanism underlying *Riok2* haploinsufficiency-induced, IL-22 –induced anemia.

nature research

Corresponding author(s): Laurie H. Glimcher and Mahesh Raundhal

Last updated by author(s): Jan 18, 2021

Reporting Summary

Nature Research wishes to improve the reproducibility of the work that we publish. This form provides structure for consistency and transparency in reporting. For further information on Nature Research policies, see Authors & Referees and the Editorial Policy Checklist.

Statistics

For all statistical analyses, confirm that the following items are present in the figure legend, table legend, main text, or Methods section.

n/a	Confirmed	
☐	☒	The exact sample size (*n*) for each experimental group/condition, given as a discrete number and unit of measurement
☐	☒	A statement on whether measurements were taken from distinct samples or whether the same sample was measured repeatedly
☐	☒	The statistical test(s) used AND whether they are one- or two-sided *Only common tests should be described solely by name; describe more complex techniques in the Methods section.*
☒	☐	A description of all covariates tested
☐	☒	A description of any assumptions or corrections, such as tests of normality and adjustment for multiple comparisons
☐	☒	A full description of the statistical parameters including central tendency (e.g. means) or other basic estimates (e.g. regression coefficient) AND variation (e.g. standard deviation) or associated estimates of uncertainty (e.g. confidence intervals)
☐	☒	For null hypothesis testing, the test statistic (e.g. *F*, *t*, *r*) with confidence intervals, effect sizes, degrees of freedom and *P* value noted *Give P values as exact values whenever suitable.*
☒	☐	For Bayesian analysis, information on the choice of priors and Markov chain Monte Carlo settings
☒	☐	For hierarchical and complex designs, identification of the appropriate level for tests and full reporting of outcomes
☐	☒	Estimates of effect sizes (e.g. Cohen's *d*, Pearson's *r*), indicating how they were calculated

Our web collection on statistics for biologists contains articles on many of the points above.

Software and code

Policy information about availability of computer code

Data collection	FACS Diva (BD Biosciences) for flow cytometry, QuantStudio 6 Flex for qRT-PCR. Details regarding data collection for proteomics and RNA-Seq are included in the Methods section of this manuscript.
Data analysis	FlowJo v9 (TreeStar) for flow cytometry ; Graph Pad Prism v8 (GraphPad) for statistical analyses; Bowtie (Version 1.2.8) was used for analyzing RNA-Seq data. GSEA v4.0.2, MSigDB v7.1, and MetaCore v20.1 build 7000 (Clarivate Analytics) for in silico analyses of proteomics and RNA-Seq datasets. Il22 promoter analysis for p53 binding sites was performed using Lasagna-Search 2.0. Other technical details regarding data analysis of the proteomics and RNA-Seq datasets are included in the Methods section of this manuscript.

For manuscripts utilizing custom algorithms or software that are central to the research but not yet described in published literature, software must be made available to editors/reviewers. We strongly encourage code deposition in a community repository (e.g. GitHub). See the Nature Research guidelines for submitting code & software for further information.

Data

Policy information about availability of data

All manuscripts must include a data availability statement. This statement should provide the following information, where applicable:

- Accession codes, unique identifiers, or web links for publicly available datasets
- A list of figures that have associated raw data
- A description of any restrictions on data availability

The original mass spectra may be downloaded from MassIVE (http:\\massive.ucsd.edu),MSV000085287. Raw RNA-Seq data is accessible via Gene Expression Omnibus (GEO) under the accession code GSE165467. Source data for all applicable figures (Main and Extended) are provided with the paper. The remaining data supporting the findings of this study are available from the corresponding authors upon reasonable request. Materials will be provided with material transfer agreements (MTA) as appropriate. All other data that support the findings of this study are available from the corresponding authors upon reasonable request.

Field-specific reporting

Please select the one below that is the best fit for your research. If you are not sure, read the appropriate sections before making your selection.

☒ Life sciences ☐ Behavioural & social sciences ☐ Ecological, evolutionary & environmental sciences

For a reference copy of the document with all sections, see nature.com/documents/nr-reporting-summary-flat.pdf

Life sciences study design

All studies must disclose on these points even when the disclosure is negative.

Sample size	No statistical tests were used to predetermine sample size. Sample size was determined based on similar previous studies reported in the literature (Schneider RKM, et al. Nature Medicine 2016). 3 -6 mice per group were used for the majority of the experiments. The exact numbers per experiment are stated in Figure Legends and are visible as individual data points.
Data exclusions	No data was excluded in this manuscript.
Replication	All reported data used at least 3-6 biological replicates within experiments. Each experiment was replicated independently 2-3 times. All attempts at replication were successful.
Randomization	Mice were randomly assigned for all experiments reported. Age- and gender- matched mice were used in individual experiments. Human samples were allocated to specific experimental groups dependent on their disease status as determined by collaborating medical practitioners.
Blinding	Investigators were not blinded to group allocations during the experiment and data analysis. Since treatment and experimental analysis could not be separated, blinding of the investigators was not feasible.

Reporting for specific materials, systems and methods

We require information from authors about some types of materials, experimental systems and methods used in many studies. Here, indicate whether each material, system or method listed is relevant to your study. If you are not sure if a list item applies to your research, read the appropriate section before selecting a response.

Materials & experimental systems

n/a	Involved in the study
☐	☒ Antibodies
☒	☐ Eukaryotic cell lines
☒	☐ Palaeontology
☐	☒ Animals and other organisms
☐	☒ Human research participants
☒	☐ Clinical data

Methods

n/a	Involved in the study
☒	☐ ChIP-seq
☐	☒ Flow cytometry
☒	☐ MRI-based neuroimaging

Antibodies

Antibodies used

Target, Clone, Cat
FLOW CYTOMETRY
BioLegend
PerCP/Cyanine5.5 anti-mouse CD3ε Antibody, 145-2C11, 100328
PerCP/Cyanine5.5 anti-mouse CD5 Antibody, 53-7.3, 100624
PerCP/Cyanine5.5 anti-mouse Ly-6G/Ly-6C (Gr-1) Antibody, RB6-8C5, 108428
PerCP/Cyanine5.5 anti-mouse/human CD11b Antibody, M1/70, 10122
PerCP/Cyanine5.5 anti-mouse/human CD45R/B220 Antibody, RA3-6B2, 103236
Brilliant Violet 421™ anti-mouse CD71 Antibody, RI7217, 113813
FITC anti-mouse CD71 Antibody, RI7217, 113806
APC anti-mouse TER-119/Erythroid Cells Antibody, TER-119, 116212
Brilliant Violet 605™ anti-mouse TER-119/Erythroid Cells Antibody, TER-119, 116239
PE Donkey anti-rabbit IgG (minimal x-reactivity) Antibody, Poly4064, 406421
PE/Cy7 anti-human CD4 Antibody, RPA-T4, 300512
FITC Annexin V, Clone N/A, 640905
PE/Cy7 anti-mouse Ly-6C Antibody, HK1.4, 128018
Brilliant Violet 650™ anti-mouse Ly-6G Antibody, 1A8, 127641
Brilliant Violet 510™ anti-mouse CD117 (c-Kit) Antibody, 105839
Brilliant Violet 650™ anti-mouse CD150 (SLAM) Antibody, 115932
Brilliant Violet 711™ anti-mouse Ly-6A/E (Sca-1) Antibody, 108131

BD Biosciences
BUV737 Rat Anti-Mouse CD16/CD32, 2.4G2, 565272
PE-CF594 Rat Anti-Mouse CD135, Clone A2F10.1, 562537
BV786 Rat Anti-Mouse CD105, Clone MJ7/18, 564746
BV605 Rat Anti-Mouse CD90.2, Clone 53-2.1, 563008

MilliporeSigma
Uncojungated IL-22RA-1 antibody, Clone N/A, 061077I
Mouse IgG, Clone N/A, 12-371

Novus Biologicals
Alexa Fluor 700 S100A8 Antibody, 63N13G5, NBP2-27067AF700
PE IL-22R alpha 1 Antibody, 496514, FAB42941P

Cell Signaling Technology
PE S100A9, D3U8M, 93941
AF647 p53, 1C12, 2533S

Thermo Fisher Scientific
IL-22 Monoclonal Antibody (1H8PWSR), PE, 12-7221-82
APC IL-22 Monoclonal Antibody, IL22JOP, 17-7222-82
PE-Cyanine7, Ki-67 Monoclonal Antibody, SolA15, 25-5698-82
FITC CD127 Monoclonal Antibody, A7R34, 11-1271-85
eFluor 660 CD34 Monoclonal Antibody, RAM34, 50-0341-82
FITC CD45.1 Monoclonal Antibody, A20), 11-0453-85
PE, CD45.2 Monoclonal Antibody, 104, 12-0454-82
eFluor 660, IL-23 p19 Monoclonal Antibody. fc23cpg, 50-7023-82

NEUTRALIZATION
Thermo Fisher Scientific
IL-22 Monoclonal Antibody, IL22JOP, 16-7222-82
Rat IgG2a kappa Isotype Control, eBR2a, 16-4321-85

CHROMATIN IMMUNOPRECIPITATION
Santa Cruz Biotechnology
Anti-p53, DO-1, SC-126 X

Validation

All commercially available antibodies used in this study are routinely tested by the respective manufacturer. Related technical data sheets can be obtained from the manufacturer's website using the catalog number provided above.

Animals and other organisms

Policy information about studies involving animals; ARRIVE guidelines recommended for reporting animal research

Laboratory animals

Wild-type C57BL/6J mice (Stock no. 000664), Vav-icre mice (Stock no. 008610), R26-CreErt2 mice (Stock no. 008463), Il22ra1-floxed (Stock no. 031003), CD45.1 C57BL/6J mice (Stock no. 002014), Trp53-/- (Stock no. 002101), Cd4-cre (Stock no. 022071), and ApcMin (Stock no. 002020) were purchased from The Jackson Laboratory (Bar Harbor, ME). Riok2-floxed mice were generated by the authors of this study. Il22 -/- mice were provided by Dr. Rachel Caspi (National Institutes of Health, Bethesda, MD) with permission from Genentech (San Francisco, CA). Epor-cre mice were a gift from Dr. Ursula Klingmüller (Deutsches Krebsforschungszentrum (DFKZ), Germany). Il22-tdtomato (Catch-22) mice were a gift from Dr. Richard Locksley (University of California at San Francisco, CA). Rps14-floxed mice were a gift from Dr. Benjamin Ebert (DFCI, Boston, MA).
Mice within each experiment were age- and sex- matched. Experiments involving young mice were performed 8-12 wk old mice. Experiments involving old mice were performed with mice 60 wks and older.

Wild animals

This study did not involve wild animals.

Field-collected samples

This study did not involve field-collected samples.

Ethics oversight

Animal procedures were approved and performed according to the Institutional Animal Care and Use Committee (IACUC) at Dana-Farber Cancer Institute (DFCI).

Note that full information on the approval of the study protocol must also be provided in the manuscript.

Human research participants

Policy information about studies involving human research participants

Population characteristics

Human research participants included in this study were aged 18 years and above with male and female representation.

Population characteristics	Genotype information is provided in Supplementary Table 2. For MDS patients, the categories were del(5q) and non-del(5q) MDS. For CKD patients, the categories were CKD patients with anemia and CKD patients without anemia based on their hemoglobin quantification.
Recruitment	Participants were not specifically recruited for this study and represent a subpopulation of all-comers (dependent on consent) seeking diagnoses or treatment for either MDS or CKD. Self-selection bias does not exist as the participants were not actively recruited for thi study and participants involvement rested solely on receiving informed consent from the participant.
Ethics oversight	MDS and CKD patient samples were collected under Institutional Review Board (IRB)-approved protocols at DFCI and Brigham and Women's Hospital (BWH), respectively.

Note that full information on the approval of the study protocol must also be provided in the manuscript.

Flow Cytometry

Plots

Confirm that:

☒ The axis labels state the marker and fluorochrome used (e.g. CD4-FITC).

☒ The axis scales are clearly visible. Include numbers along axes only for bottom left plot of group (a 'group' is an analysis of identical markers).

☒ All plots are contour plots with outliers or pseudocolor plots.

☒ A numerical value for number of cells or percentage (with statistics) is provided.

Methodology

Sample preparation	Whole bone marrow (BM) cells were isolated by crushing hind leg bones (femur and tibia) with mortar and pestle in staining buffer (PBS (Corning) supplemented with 2% heat-inactivated fetal bovine serum (FBS, Atlanta Biologicals) and EDTA (GIBCO). Whole BM was lysed with 1X PharmLyse (BD Biosciences) for 90 s, and the reaction was terminated by adding an excess of staining buffer. Cells were labeled with fluorochrome-conjugated antibodies in staining buffer for 30 min at 4 ℃. For flow cytometric analysis, cells were incubated with combinations of fluorochrome-conjugated antibodies to the following cell surface markers: CD3 (17A2), CD5 (53–7.3), CD11b (M1/70), Gr1 (RB6–8C5), B220 (RA3–6B2), Ter119 (TER119), CD71 (C2), c-kit (2B8), Sca-1 (D7), CD16/32 (93), CD150 (TC15–12F12.2), CD48 (HM48-1). For sorting of lineage-negative cells, lineage markers included CD3, CD5, CD11b, Gr1 and Ter119. For sorting erythroid progenitor cells, the lineage cocktail did not include Ter119. All reagents were acquired from BD Biosciences, Thermo Fisher Scientific, Novus Biologicals, Tonbo Biosciences, or BioLegend. Identification of apoptotic cells was carried out using the Annexin V Apoptosis Detection Kit (BioLegend). Intracytoplasmic and intranuclear staining was performed using Foxp3/Transcription Factor Staining Kit (Thermo Fisher Scientific) or 0.1% saponin in PBS supplemented with 3% FBS. For staining performed with AF647 p53 antibody (Cell Signaling Technology), cells were permeabilized with 90% ice-cold methanol. To increase the sorting efficiency, whole BM samples were lineage-depleted using magnetic microbeads (Miltenyi Biotec) and autoMACS Pro magnetic separator (Miltenyi Biotec). Cell sorting was performed on a FACS Aria flow cytometer (BD Biosciences), data acquisition was performed on a BD Fortessa X-20 instrument equipped with 5 lasers (BD Biosciences) employing FACSDiva software. Data were analyzed by FlowJo (Tree Star) version 9 software. Flow analyses were performed on viable cells by exclusion of dead cells using either DAPI or a fixable viability dye (Tonbo Biosciences). Gating for early and committed hematopoietic progenitors was performed as described elsewhere56. ILCs and NKT cells were identified as Lin–CD45+CD90+CD12+ and CD3e+ NK1.1+, respectively.
Instrument	BD Fortessa for data collection, BD FACS ARIA II for cell sorting
Software	FlowJo v9 (TreeStar), BD FACS Diva
Cell population abundance	Sorted populations were assessed for purity by post-sort analysis on BD FACS ARIA II. Purity of over 95% was routinely achieved.
Gating strategy	Erythroid progenitors/precursors were gated as viable, lineage(low), CD71(+/-), Ter119(+) as shown in Extended Data Fig. 2a. Gating strategy for identification of IL-22RA1(+) cells in the bone marrow is shown in Extended Data Fig. 8a and 8b. Briefly, viable singlet cells were gated to remove lineage-positive cells and then the erythroid progenitor gate (based on CD71 and Ter119 expression) was applied. IL-22RA1 expression on cells in the erythroid progenitor gate was assessed.

☒ Tick this box to confirm that a figure exemplifying the gating strategy is provided in the Supplementary Information.